Energy Advances

ROYAL SOCIETY OF CHEMISTRY

PAPER

View Article Online
View Journal | View Issue

Check for updates

Cite this: *Energy Adv.*, 2025, 4, 1179

A multi-parameter analysis of iron/iron redox flow batteries: effects of operating conditions on electrochemical performance†

Challuri Sai Venkata Akhil Kumar, *[ab] Jens Tübke, [ab] Karsten Pinkwart [ae] and Jens Noack [acd]

Iron/iron redox flow batteries (IRFBs) are emerging as a cost-effective alternative to traditional energy storage systems. This study investigates the impact of key operational characteristics, specifically examining how various parameters influence efficiency, stability, and capacity retention. IRFB systems with a volume of 60 mL per tank (20.25 Ah L^{-1}) demonstrated superior capacity utilization, achieving a coulombic efficiency (CE) of up to 95% and an energy efficiency (EE) of 61% over 25 charge/discharge cycles. In contrast, systems with lower capacity utilization in larger electrolyte volumes (5.67 Ah L^{-1}) required more charge/discharge cycles to reach the optimal pH-induced kinetic benefits due to increased proton content. Extended charging durations of up to 8 hours facilitated complete redox conversion, enhancing CE, EE, and voltage efficiency (VE). Brief rest intervals of 5 to 10 minutes supported stable discharge capacity retention and energy efficiency throughout the cycles, while more extended rest periods (*e.g.*, 60 minutes) were associated with diminished performance, possibly due to ionic resistance buildup in the membrane or system imbalances occurring during extended idle times. Charge cutoff voltages between 1.6 and 1.65 V provided an optimal compromise between suppressing side reactions, enhancing capacity retention, and improving efficiency. The constant current–constant voltage (CCCV) method yielded better voltage efficiencies than the constant current (CC) approach when sustaining long-term cycling. Additionally, integrating a recombination cell minimized hydrogen-related losses, enhancing operational stability. These findings provide valuable insights for optimizing the operation of IRFBs in energy storage applications.

Received 22nd May 2025,
Accepted 14th July 2025

DOI: 10.1039/d5ya00139k

rsc.li/energy-advances

Open Access Article. Published on 14 July 2025. Downloaded on 4/18/2026 5:06:11 AM.
This article is licensed under a Creative Commons Attribution 3.0 Unported Licence.

Introduction

Redox flow batteries have emerged as promising technology for large-scale energy storage, effectively addressing the intermittency issues associated with renewable energy sources such as wind and solar.[1,2] The urgency of climate change, air pollution, and concerns about energy security have accelerated the adoption of renewable energy generation. Given the intermittent and non-dispatchable nature of wind, solar, and other renewable sources, there is a growing demand for energy storage solutions to help stabilize electrical grids and facilitate the transition to decentralized energy systems.[3] In Germany, solar and wind power account for 41.6% of electricity generation.[4] Flow batteries have gained significant attention primarily due to their scalable energy capacity, separate power and energy ratings, and long cycle life.[5,6]

Iron-based flow batteries have emerged as a promising technology for large-scale energy storage, particularly in integrating renewable energy sources into the electrical grid.[6,7] These iron-based redox flow batteries present an attractive alternative to conventional energy storage solutions due to their low cost, material abundance, and environmental compatibility.[5,6] The widespread availability of iron, which can be obtained for less than $ 0.10 per kilogram, and the ability to leverage waste products like iron sulfate, contribute to the economic viability of iron-based redox flow batteries for large-scale energy storage applications.[5,6,8] The operational mechanism of all-iron redox flow batteries differs significantly

[a] *Applied Electrochemistry, Fraunhofer Institute for Chemical Technology ICT, 76327 Pfinztal, Germany. E-mail: akhil.challuri@ict.fraunhofer.de*
[b] *Karlsruhe Institute of Technology (KIT) Institute for Mechanical Process Engineering and Mechanics, Geb. 30.70, Straße am Forum 8, 76131 Karlsruhe, Germany*
[c] *Australian Institute for Bioengineering and Nanotechnology, The University of Queensland (UQ), Brisbane QLD, 4072, Australia*
[d] *Universität der Bundeswehr München, Fakultät elektrische Energiesysteme und Informationstechnik (EIT), Werner-Heisenberg-Weg 39, 85579 Neubiberg, Germany*
[e] *Hochschule Karlsruhe – University of Applied Sciences, Faculty of Electrical Engineering and Information Technology, Moltkestraße 30, 76133 Karlsruhe, Germany*
† Electronic supplementary information (ESI) available. See DOI: https://doi.org/10.1039/d5ya00139k

© 2025 The Author(s). Published by the Royal Society of Chemistry

Open Access Article. Published on 14 July 2025. Downloaded on 4/18/2026 5:06:11 AM. This article is licensed under a Creative Commons Attribution 3.0 Unported Licence.

from that of conventional all-liquid redox flow batteries due to the presence of a solid–liquid phase transition. Specifically, the electrochemical processes involve the deposition and dissolution of metallic iron, introducing a solid phase into the energy storage system. This solid–liquid phase change makes all-iron batteries like hybrid flow batteries, such as zinc-bromine systems. A key consequence of this solid-phase involvement is the inherent coupling of energy and power scalability. The energy storage capacity, which is directly proportional to the mass of accumulated solid iron, is intrinsically linked to power delivery, which depends on the kinetics of iron deposition and dissolution. This interdependence stands in contrast to traditional all-liquid flow batteries, where the energy storage capacity, determined by the electrolyte tank volume, and power output, dictated by the electrochemical stack size, are independently scalable. Iron-based systems exhibit favourable safety profiles and environmental benefits, as they do not involve toxic materials.[9,10] Recent studies have highlighted the potential for improved performance through innovative designs and incorporating additives, such as zinc ions, which enhance the electrochemical properties of iron electrodes.[10] The open circuit voltage (OCV) for iron-based systems in deep eutectic solvents (DES) is reported to be comparable to that in aqueous electrolytes, indicating the feasibility of these systems in various environments.[11] In addition to iron-based systems, other aqueous redox flow battery technologies, such as vanadium-based,[12,13] zinc-based,[1,14,15] and alternative iron-based[5,6,9,16,17] systems, have also garnered significant research interest.

The IRFB battery was discovered in 1981 by Hruska *et al.* and uses a reactant pair composed of three different oxidation states of a single element to prevent irreversible reactant loss.[18] The half-cell reactions for the iron-redox battery can be expressed as follows:[5,19,20]

$$Fe^{2+}_{(aq)} \rightleftharpoons Fe^{3+}_{(aq)} + e^- \quad \phi^{0,+} = +0.77\ V \qquad (1)$$

$$Fe^{2+}_{(aq)} + 2e^- \rightleftharpoons Fe_{(s)} \quad \phi^{0,-} = -0.44\ V \qquad (2)$$

$$3Fe^{2+}_{(aq)} \rightleftharpoons Fe_{(s)} + 2Fe^{3+}_{(aq)} \quad \phi_{cell} = 1.21\ V \qquad (3)$$

The working principle of the iron-redox flow battery involves the conversion between ferrous (Fe^{2+}) and ferric (Fe^{3+}) ions during charging and discharging. During charging, the ferrous ions (Fe^{2+}) are oxidized to ferric ions (Fe^{3+}) at the positive electrode, and the reverse reaction occurs during discharge at the same electrode. A critical challenge in iron-based redox flow batteries is the risk of capacity degradation due to the crossover of soluble Fe^{3+} ions through the membrane.[1,5] Researchers have recently focused on improving the performance of iron-based redox flow batteries, particularly in terms of energy efficiency and cycle life, which are critical factors for their commercial viability.[5,8]

A key focus area in developing IRFBs is the investigation of electrolyte additives and their influence on the system's electrochemical performance. Researchers have explored the addition of various electrolyte additives, including acids, chelating agents, and organic compounds, to enhance the reversibility and stability of the Fe/Fe^{2+} redox reaction.[5] For instance, the inclusion of oxalic acid as an electrolyte additive has been shown to improve the energy efficiency and cycle life of IRFBs by stabilizing the Fe species and reducing the overpotential for the Fe/Fe redox reaction, Interestingly, the use of organic compounds like 2,2′-bipyridine as electrolyte additives has also been investigated as a strategy to enhance the kinetics and reversibility of the Fe/Fe^{2+} redox reaction, ultimately leading to improvements in the overall energy efficiency and cycle life of the system.[5] Prof. Savinell's group has been instrumental in exploring the electrochemical performance of iron–ligand complexes, which can enhance the stability and efficiency of all-iron RFBs. Their studies demonstrate that the use of specific ligands can significantly improve the coulombic efficiency of iron plating, thus addressing one of the critical challenges in the commercialization of these batteries.[21]

The introduction of various other electrolyte additives has also been explored to mitigate issues such as capacity retention and electrolyte degradation, which are critical factors affecting the long-term stability and performance of IRFBs.[22] Moreover, the development of membranes with improved ionic selectivity and reduced crossover rates is critical for minimizing parasitic reactions and enhancing the efficiency and longevity of iron-based redox flow battery systems.[23] First-principles studies have indicated that controlling the pH levels within the system, alongside optimizing ionic conductivity through specific membrane selections, can lead to pronounced improvements in coulombic efficiency and overall charge–discharge capabilities.[23,24] A significant advancement is the development of slurry electrodes, which improve the distribution of active materials and effectively tackle the issues related to solid electrodes, such as the plating reactions during charging cycles. Furthermore, the adoption of three-dimensional electrode designs has exhibited encouraging results in enhancing the interfacial area and enabling rapid electron transfer kinetics, thereby elevating overall battery efficiency. Creative structural innovations in electrode arrangements have been essential to these progressions. Specifically, using slurry electrodes has improved material distribution and alleviated challenges associated with solid electrodes during charging cycles. In addition, the integration of three-dimensional electrode structures has shown considerable promise in enhancing the interfacial area and facilitating effective electron transfer, ultimately enhancing battery performance.[22,25]

In conjunction with optimal electrolyte selection and electrode modification, investigating hydrogen recombination processes is crucial for improving the operational efficiency of iron–hydrogen RFBs. Recent studies, particularly by Selverston *et al.*, elaborated on the dynamic interactions between hydrogen and ferric ions in recombination reactions. Their work highlighted an in-tank hydrogen and ferric ion recombination method that could streamline hydrogen utilization and improve overall energy efficiency in iron RFBs.[26] This work demonstrates the feasibility of a membraneless design to optimize hydrogen cycling, thereby enhancing the

© 2025 The Author(s). Published by the Royal Society of Chemistry

Open Access Article. Published on 14 July 2025. Downloaded on 4/18/2026 5:06:11 AM. This article is licensed under a Creative Commons Attribution 3.0 Unported Licence.

electrochemical performance of the systems. The impact of design choices on the efficiency of hydrogen recombination is further supported by research conducted by Noack *et al.* Their investigations into Fe/Fe redox flow batteries revealed that the electrochemical reversibility of the Fe^{2+}/Fe^{3+} reactions play a pivotal role in battery efficiency. They have focused on developing a hydrogen–ferric ion rebalance cell that operates at low hydrogen concentrations to address the adverse effects of hydrogen evolution on the capacity of iron-based redox flow batteries during long-term operation, thereby ensuring safe and reliable battery performance.[19] The increasing pH, a byproduct of hydrogen formation, encourages iron deposition, resulting in capacity loss caused by the precipitation of iron hydroxide.[6,19,27] Further complications arise from electrode and fluidic system precipitates, elevating internal resistance and risking battery failure. Consequently, in subsequent property tests, the continued utilization of this recombination cell was decided upon. The continued use of the recombination cell in subsequent experiments facilitated a comprehensive examination of battery properties, providing valuable insights for the progression of iron/iron redox flow battery technology.[28] The reactions in recombination cells are written below:[19,29]

$$2Fe^{3+}_{(aq)} + e^- \rightarrow 2Fe^{2+}_{(aq)} \quad \phi^{0,+} = +0.77\ V \tag{4}$$

$$2H^+_{(aq)} + 2e^- \rightarrow H_{2(g)} \quad \phi^{0,-} = 0\ V \tag{5}$$

$$H_{2(g)} + 2Fe^{3+}_{(aq)} \rightarrow 2H^+_{(aq)} + 2Fe^{2+}_{(aq)} \quad \phi_{cell} = 0.77\ V \tag{6}$$

Despite the progress in enhancing iron-based redox flow batteries, their widespread adoption for large-scale energy storage remains limited due to the complex interplay of operational parameters affecting their electrochemical performance and long-term stability. For instance, in vanadium redox flow batteries (VRFBs), studies have demonstrated the critical influence of operating parameters like flow rates and state of charge on energy efficiency and capacity retention.[30,31] Similarly, zinc-based flow batteries have shown that the choice of membrane and electrolyte composition directly impacts coulombic efficiency and cycle life.[32] Building on these findings, researchers have explored strategies to optimize the operational conditions in alternative systems, including electrolyte formulations and electrode design, which have led to significant improvements in stability and performance.[33,34]

For iron-based redox flow batteries, factors such as capacity utilization, rest times, charge/discharge cutoff voltages, the application of constant current-constant voltage (CCCV) charging protocols, and the influence of self-discharge remain underexplored yet crucial for maximizing their efficiency and reliability. Addressing these parameters is essential to overcoming challenges such as capacity fading caused by iron precipitation and membrane crossover. To fill this gap, this study provides a multi-parameter analysis of these conditions and their effects on environmentally friendly and secure iron/iron redox flow battery systems. This research contributes to developing scalable and sustainable solutions for large-scale energy storage by leveraging insights from other systems and applying them to iron-based technologies.

Experimental procedure

A solution of 1.5 M $FeCl_2$, 2 M NH_4Cl, and 0.2 M HCl with a pH < 0 served as an energy storage medium. The $FeCl_2{\cdot}4H_2O$ was supplied from Carl Roth GmbH, Germany, with a purity of $\geq$99%. With the help of Faraday's law, the theoretical capacity of the electrolyte volume was calculated. The electrolyte tanks of the iron/iron redox flow battery were filled with a 1 : 1 volume (negative/positive) ratio solution. A test stand was set up for properties analysis, as shown in the schematic diagram in Fig. 1(a). The test stand consisted of an iron/iron redox flow cell with a recombination cell and two tanks for the energy storage medium. A dual-line pump and Gamry reference 3000 potentiostat were included in the setup for electrolyte purging and cell analysis. The iron/iron redox flow cell was electrically connected to the potentiostat, but the recombination cell was short-circuited. The electrolyte was purged into different cells (iron and recombination cells) so that gaseous hydrogen from the negative storage tank's headspace can reach the recombination cell's negative half-cell. The output of the positive energy storage medium of the Fe/Fe-RFB cell (Fe^{3+}/Fe^{2+}) was connected to the input of the positive half-cell of the recombination cell. The electrolyte was returned to the positive storage tank after passing the recombination cell. A 100 mm high water column closed the outlet connection of the recombination cell's hydrogen side.

The iron/iron redox flow cell in Fig. 1(b) includes two half-cells with an active area of 40 cm^2 separated by an anion-exchange membrane (FUMASEP - 450, Fumatech GmbH, Germany). The end plate on the positive half-cell has been fitted with the necessary flow connections and an attached insulation plate for electrical insulation support. The positive half-cell consisted of a flow frame in which a Graphite bi-polar plate (Schunk Group, Germany) with a thickness of 3 mm was embedded for electrical contact between the half-cell and the current collector. The gap between the frame and the carbon plate has been sealed with conventional silicone sealant. A thermally treated carbon felt (GFA 4.6 EA, SGL - Carbon, Germany) was placed in the flow frame to increase the electrochemical surface area. The negative half-cell also consisted of a polyvinyl chloride (PVC) flow frame with an embedded graphite bi-polar plate. In the iron deposition process, a substrate material forming carbon fabric (ACC-507-20, Kynol Europa GmbH) was strategically positioned within the flow frame. The flow frames in both half-cells were designed to regulate uniform electrolyte distribution. On the positive side of iron/iron flow cell, the flow-through configuration allowed the electrolyte to pass uniformly through the carbon-felt electrode, maximizing electrochemical activity. A flow-by design was employed on the negative side of the iron/iron flow cell, where the electrolyte flowed over the carbon fabric substrate positioned in the flow frame. Additionally, a 3D-printed spacer was

Open Access Article. Published on 14 July 2025. Downloaded on 4/18/2026 5:06:11 AM.
This article is licensed under a Creative Commons Attribution 3.0 Unported Licence.

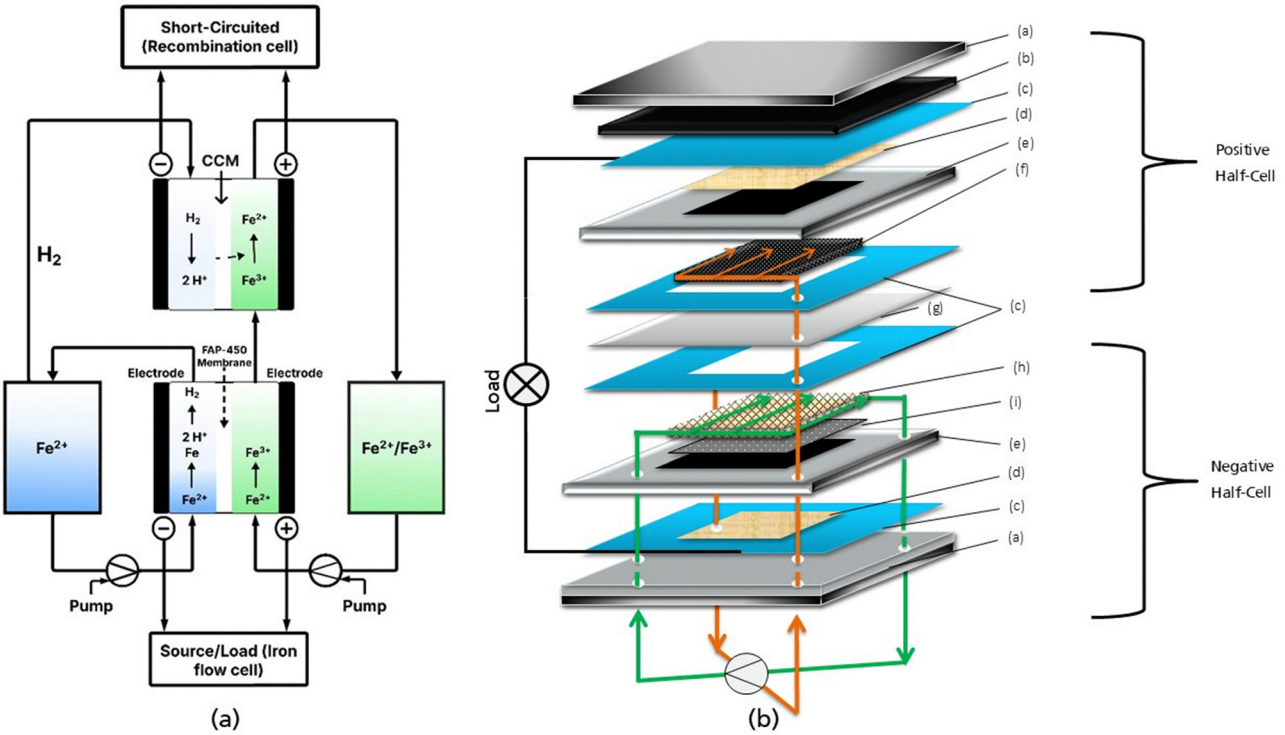

Fig. 1 (a) Schematic diagram of an iron/iron redox flow battery with recombination cell. The reactions in the figure represent charging process, (b) exploded cross-sectional view of the iron/iron flow cell, showing key components including end plates (a), insulation plates (b), gaskets (c), copper plates (d), flow frame with bipolar plates (e), carbon felt (f), anion-exchange membrane (g), spacer (h) and carbon fabric (i). Panel (b) adapted and modified from Noack, J. *et al.*, *J. Electrochem. Soc.*, 2020, **167**, 160527, under CC BY 4.0.

integrated into the negative half-cell flow frame to form a well-defined cavity that facilitates uniform iron deposition (Fig. 2). The spacer, fabricated from chemically resistant acrylonitrile butadiene styrene (ABS) features a grid-like top structure (87 mm × 62 mm) and a total height of 3.5 mm, resulting in an effective cavity thickness of approximately 3.3–3.4 mm. This structured geometry aids in promoting consistent electrolyte distribution and mechanical stabilization of the deposition surface throughout repeated cycling. Gasket seals were used to prevent the electrolyte from getting between layers and at the connection points of the flow channels exit. Thin copper sheets were used as current collectors. Finally, the two end plates were placed on the stack carefully, and the 13 screws were inserted into the existing holes of the end plates and tightened with the nuts.

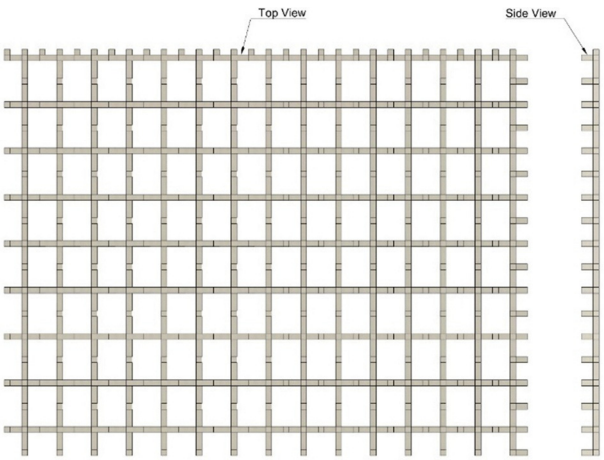

Fig. 2 Top and side view schematic of the 3D-printed spacer inserted in the negative half-cell. The top view illustrates the open-grid design used to form localized cavities for iron deposition. The side view shows the spacer's position relative to the carbon fabric and membrane.

The recombination cell was constructed similarly to the iron/iron redox flow cell with flow-through design. It consisted of two half-cells separated by a one-sided catalyst-coated membrane (CCM) (NAFION 115, 1 mg cm^{-2} Pt/C, Baltic Fuel Cells, Germany). The membrane's catalyst layer was only on the negative half-cell, the negative electrode where the hydrogen reaction occurred. Two toray papers and a glass carbon foam (ERG Aerospace, USA) were placed into the negative half-cell flow frame cavity to make electrical contact between the catalyst coating and the bipolar plate. The positive half-cell flow frame used a thermally treated carbon felt (GFA 4.6 EA, SGL - Carbon, Germany). The end plates stabilize the structure and produce the necessary contact pressure. Thin copper plates served as current collectors on both sides. Different flat gaskets sealed the cell. Two steel plates held components together, one of which had media feedthroughs.

This study systematically examined the influence of various operational parameters on the performance of iron/iron redox

© 2025 The Author(s). Published by the Royal Society of Chemistry

Open Access Article. Published on 14 July 2025. Downloaded on 4/18/2026 5:06:11 AM.
This article is licensed under a Creative Commons Attribution 3.0 Unported Licence.

flow batteries (RFBs). Electrolyte volume, ranging from 60 to 300 mL with a maximum theoretical capacity density of 20.25 Ah L^{-1}, was examined to discern its impact on system efficiency, yielding insights into optimal operational ranges. Capacity utilization, investigated through varying charging times from 0.5 to 8 hours (max. theoretical capacity utilization 6.25–100%), provided an understanding of the dynamic interplay shaping battery behaviour. Rest time intervals, ranging from 5 to 60 minutes, were explored to identify optimal durations enhancing system efficiency and longevity. Charge and discharge cut-off voltages were systematically varied from 1.55 to 1.9 V and 0.6 to 0 V, respectively. This investigation offered initial insights into voltage thresholds influencing the stability and performance of iron/iron RFBs. A comparative analysis of constant current (CC) and constant voltage (CV) methodologies enhanced the understanding of the subtle differences in charge and discharge processes. Exploring initial self-discharge implications on iron/iron RFBs addressed concerns in energy storage applications. The recombination cell was incorporated into the test stand with the iron/iron redox flow cell for all experiments performed in this study.

For each series of parameter experiments, including variations in electrolyte volume, charging times, rest intervals, cutoff voltages, constant current (CC) *versus* constant voltage (CCCV) cycling, and self-discharge tests, a completely new iron/iron redox flow cell and recombination cell were assembled. New materials were utilized for every assembly, including new membranes, copper plates, and electrodes for both cells, with the exception of the catalyst-coated membrane (CCM) and electrode materials in negative half-cell of recombination cell. A newly prepared Fe^{2+} electrolyte solution was employed before each experiment to mitigate oxidation-related issues and ensure consistency. For example, during the electrolyte volume experiments (which ranged from 60 to 300 mL), a newly constructed iron/iron redox flow cell was assembled, and a newly prepared Fe^{2+} electrolyte was introduced for each specific electrolyte volume experiment. The electrolyte was completely removed after each experiment, which included over 25 charge/discharge cycles of 1-hour charge and discharge until 0 V at a current density of 25 mA cm^{-2} with 5 minutes of rest between each phase. A new Fe^{2+} solution was then prepared and filled with electrolyte tanks for the subsequent test. Before moving forward, electrochemical impedance spectroscopy (EIS) was conducted to verify the internal resistance and confirm that it remained within an anticipated range of 80–120 mOhms. After completing the electrolyte volume experimental series, the entire flow cell comprising electrodes and membranes was removed and rebuilt to eliminate any potential carryover effects. Each parameter series, individually subjected to five values, underwent a minimum of two experiments with standard deviations, reinforcing the reliability and robustness of the study's findings. This protocol was consistently followed to across all experimental series by changing their parameters ensuring the reproducibility and reliability of the electrochemical performance data. All experiments were conducted at room temperature.

Iron deposition and volumetric electrode utilization calculations

The mass of iron deposited on the electrode during each charge cycle was estimated using Faraday's law of electrolysis, assuming a 100% charge-to-mass conversion efficiency. The formula used is as follows:

$$m_{Fe} = \frac{Q \cdot M_{Fe}}{n \cdot F} \quad (7)$$

where Q is the total charge passed (in Coulombs), M_{Fe} = 55.85 g mol^{-1} is the molar mass of iron, n = 2 is the number of electrons involved in the Fe^{2+}/Fe^{0} redox reaction, and F = 96 485 C mol^{-1} is the Faraday constant. The charge Q was calculated from the applied current (1 A) and charge duration (in seconds). The volumetric electrode utilization (%) was calculated by dividing the mass of deposited iron by the total theoretical pore volume of the carbon felt electrode (40 cm^2 × 3 mm thickness) and assuming a bulk iron density of 7.87 g cm^{-3}. These calculations were performed for each experiment using the 25th charge/discharge cycle data.

$$\text{Volumetric utilization}\,(\%) = \left(\frac{m_{Fe}}{V_{felt} \cdot \rho_{Fe}}\right) \times 100 \quad (8)$$

Results and discussion

Discussion of a cycle example during CCCV charge/discharge

The charge and discharge voltage profiles of the iron/iron redox flow battery (IRFB) over an 18 - hour period provide an understanding of the battery's electrochemical behaviour and performance characteristics, as illustrated in Fig. 3. In this detailed representation, the voltage (shown as a blue curve) and current

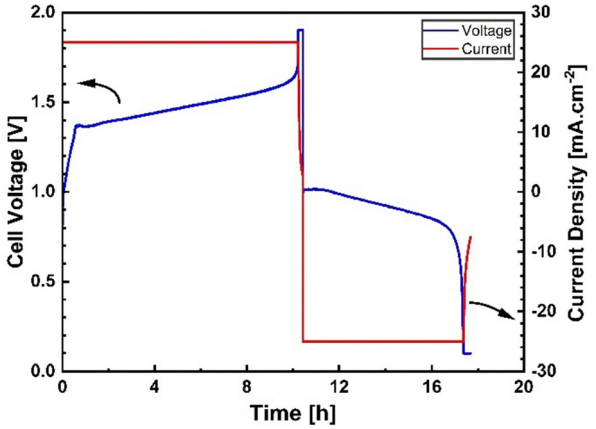

Fig. 3 Charge/discharge cycle of an iron/iron redox flow battery using the constant current constant voltage (CCCV) method. The data shown corresponds to the first cycle, with voltage and current density plotted as a function of time. The experiment was conducted at room temperature with an electrolyte volume of 200 : 200 mL (theoretical capacity = 8.01 Ah). The electrolyte composition was 1.5 M $FeCl_2$, 2 M NH_4Cl, and 0.2 M HCl. The charge/discharge process employed a rest period of 5 minutes, cutoff voltages of 1.9 V and 0 V, and a 25-mA cm^{-2} current density.

Open Access Article. Published on 14 July 2025. Downloaded on 4/18/2026 5:06:11 AM. This article is licensed under a Creative Commons Attribution 3.0 Unported Licence.

density (depicted as a red curve) are mapped against time while operating under constant current-constant voltage (CCCV) conditions. The cut-off voltages are set at 1.9 V for charging and 0.1 V (near to 0% SOC) for discharging to protect battery deep discharge. Throughout both the charge and discharge cycles, a steady current density of 25 mA cm^{-2} is maintained, with a strategically incorporated rest period of 5 minutes between each cycle, allowing the battery to stabilize and reduce potential fluctuations in performance.

At the onset of the charging phase, the voltage rises sharply from 0 V to approximately 1.5 V. The transient increase in voltage is primarily caused by the high initial resistance associated with the absorption of iron ions by the carbon electrode before the system stabilizes.[19] As the charging continues, the voltage increases steadily from around 1.5 V until it reaches the predetermined cut-off voltage of 1.9 V. This gradual ascent reflects the electrochemical reduction of Fe^{2+} to metallic iron (Fe) at the anode (negative half-cell). Simultaneously, Fe^{2+} ions are oxidized to Fe^{3+} at the cathode (positive half-cell) during the charging phase. When the voltage is cut off at 1.9 V, the battery transitions into the charging protocol's constant voltage (CV) phase. During this critical phase, the voltage remains capped at 1.9 V, while the current density experiences a significant decrease, dropping to approximately 2.5 mA cm^{-2}. This decline in current density indicates the battery is nearing full charge and is an important measure to prevent overcharging, thereby extending the battery's lifespan. It is important to highlight that while the theoretical capacity was 8.01 Ah, the observed charge capacity exceeded this number due to parasitic side reactions, primarily hydrogen evolution at the negative electrode. These reactions become more pronounced during the constant-voltage (CV) phase, where the applied potential continues to drive current even after the main iron redox conversion has concluded. As the current gradually diminishes to low levels, the extended CV period results in additional charge input that is not associated with productive energy storage but rather with side reactions and polarization losses inherent to the iron redox flow battery (IRFB) system.

A 5-minute rest period was implemented between the charge and discharge phases to allow the battery system to stabilize. This interval facilitates electrolyte equilibration and minimizes transient effects, thereby enhancing the reliability of the subsequent performance data. At the start of the discharge phase, a rapid voltage drop occurs, falling from 1.9 V to approximately 1.0 V. This immediate decline is characteristic of the transition from the open-circuit voltage (OCV) state to the application of a discharge current, reflecting the internal resistance and activation overpotentials within the cell. As the discharge continues, the voltage gradually decreases due to the consumption of active materials and an increase in internal resistance. This trend becomes particularly pronounced after about 4 hours of discharge. Initially, the current density is relatively high, around -25 mA cm^{-2}, but it decreases to approximately -7.5 mA cm^{-2} as the battery enters the constant voltage (CV) phase. The short duration of the CV phase following discharge is primarily due to the rapid depletion of electroactive species and the battery's limited capacity to sustain a constant voltage once most of the stored energy has been released. As the concentration of reactants decreases, the cell's ability to maintain the set voltage diminishes, leading to a quick conclusion of the CV phase. Towards the end of the discharge cycle, the voltage steadily declines until it reaches the lower cut-off threshold of 0.1 V. This cut-off point serves as a protective measure to prevent deep discharge, which could compromise the structural integrity of the cell and reduce its operational lifespan.

The voltage profile observed during the discharge cycle, including the initial rapid drop, gradual decline, and short CV phase, offers insights into the electrochemical dynamics and efficiency of the IRFB system. Understanding these behaviors is crucial for optimizing battery performance and longevity. These recorded voltage curves tailored to specific parameters were utilized to analyze coulombic efficiency (CE), energy efficiency (EE), voltage efficiency (VE), and capacities across 25 cycles in all parameter-based experiments, providing insights into the IRFB's electrochemical properties.

Effect of capacity utilization on iron/iron redox flow batteries

Influence of electrolyte volume on capacity utilization under fixed charge/discharge duration. In Fig. 4(a)–(d), the discharge capacity, coulombic, energy, and voltaic efficiencies of the IRFBs are shown as a function of the number of charge/discharge cycles for varying electrolyte volumes of 60 mL, 100 mL, 150 mL, 200 mL, and 300 mL. The experiments were carried out using a 40 cm^2 lab cell with a charging time of one hour (maximum capacity utilization - 41.15%) and a maximum discharge time of one hour per cycle. However, due to varying total electrolyte volumes, each configuration resulted in a different theoretical maximum capacity ($Q_{max,theo}$), ranging from 2.43 Ah (60 mL) to 12.06 Ah (300 mL). Experiments for each electrolyte volume were conducted twice to ensure statistical robustness, and mean values with standard deviations were calculated.

The initial discharge cycle for the 60 mL electrolyte volume (20.25 Ah L^{-1}) in Fig. 4(a) achieved a discharge capacity of 0.69 Ah (5.75 Ah L^{-1}). This corresponds to a capacity utilization of approximately 28%, compared to a maximum capacity utilization of 41.15%, resulting in a capacity loss of around 13%. This early-cycle inefficiency was supported by Fig. S1 (ESI†), which presents data from a comparable experiment showing elevated recombination cell currents during the first ten cycles. The high recombination current is indicative of increased hydrogen evolution, likely driven by the initially low pH, which in turn reduced the discharge capacity and efficiency in early cycles. It is important to note that the hydrogen evolution reaction (HER) consumes protons (H^+), thereby gradually shifting the electrolyte pH toward more alkaline values. The 60 mL electrolyte volume experiment achieved the highest performance, reaching a discharge capacity of 0.94 Ah (7.83 Ah L^{-1}), corresponding to a capacity utilization of approximately 38.7%, with a capacity loss reduced to 2.55% and a standard deviation of 3% after 25 cycles. The findings are further supported by iron deposition

 © 2025 The Author(s). Published by the Royal Society of Chemistry

Open Access Article. Published on 14 July 2025. Downloaded on 4/18/2026 5:06:11 AM.
This article is licensed under a Creative Commons Attribution 3.0 Unported Licence.

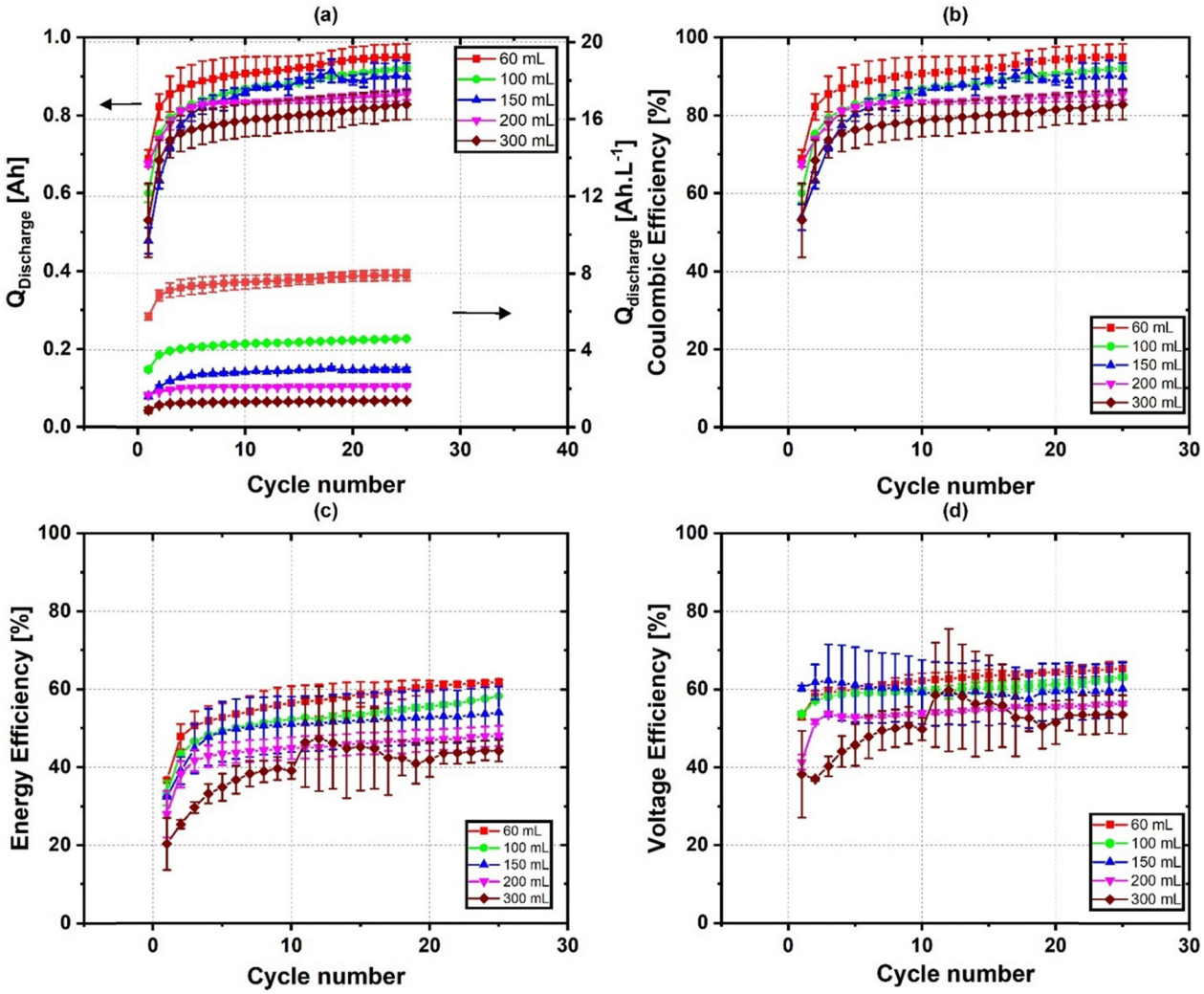

Fig. 4 Performance metrics of IRFBs with varied electrolyte volumes with constant 1-hour charge/discharge. (a) discharge capacity/specific discharge capacity *vs.* cycles, (b) coulombic efficiency *vs.* cycles, (c) energy efficiency *vs.* cycles, (d) voltage efficiency *vs.* cycles. The experiments were conducted at room temperature with a charge/discharge time of 1 hour at varied electrolyte volumes. The electrolyte composition was 1.5 M $FeCl_2$, 2 M NH_4Cl, and 0.2 M HCl. The charge/discharge process employed a rest period of 5 minutes and a current density of 25 mA cm^{-2}. All experiments are the mean of two experiments with standard deviations.

calculations (Table 1), which show that the 60 mL electrolyte experiment deposited the highest mass of iron at 1.94 g, achieving a volumetric electrode utilization of 2.05%. This improvement is attributed to relatively capacity utilization enabled by reduced proton content and more favourable pH conditions. During charging, as 1 Ah of capacity is transferred, a significant portion of protons is moved into the positive half-cell with the aid of the recombination cell, thereby increasing

Table 1 Summary of performance metrics for iron/iron redox flow batteries at the 25th cycle under varied electrolyte volumes (60–300 mL) using a theoretical capacity density of 20.25 Ah L^{-1}. All experiments were conducted under constant current conditions (25 mA cm^{-2}) with fixed 1-hour charge and discharge durations. A 5-minute rest period was applied between each charge/discharge step. The electrolyte composition was maintained at 1.5 M $FeCl_2$, 2 M NH_4Cl, and 0.2 M HCl, and all experiments were performed at room temperature. Reported values include Fe deposited, volumetric electrode utilization, capacity utilized, CE, EE, VE, and energy/capacity densities, calculated from experimentally measured discharge performance

$V_{electrolyte}$ [mL]	$Q_{theoretical}$ [Ah]	$Q_{discharge}$ [Ah]	$Fe_{deposited}$ (g)	$V_{electrode\ itilization}$ (%)	$Q_{utilized}$ [%]	Capacity density [Ah L^{-1}]	Energy density [Wh L^{-1}]	CE [%]	EE [%]	VE [%]
60	2.43	0.94	1.94	2.05	39.8	7.83	6.83	94.2	61.9	65.16
100	4.16	0.91	1.83	1.93	22.9	4.60	3.75	91.1	58.2	63.12
150	6.10	0.88	1.81	1.92	14.9	2.97	2.33	89.1	54.0	60.67
200	8.01	0.85	1.81	1.92	10.6	2.13	1.63	85.4	48.0	56.28
300	12.06	0.83	1.76	1.87	6.88	1.38	0.90	83.3	44.2	53.31

Open Access Article. Published on 14 July 2025. Downloaded on 4/18/2026 5:06:11 AM. This article is licensed under a Creative Commons Attribution 3.0 Unported Licence.

the pH in the negative half-cell and improving the kinetics of the iron redox reaction. The study shows a significant decrease in capacity loss from 12.75% in the first cycle to 2.55% by the 25th cycle, indicating a shift from an unstable state with side reactions to a more stable electrochemical environment over long-term cycling.

Larger electrolyte volume, such as 300 mL with a maximum theoretical capacity of 12.06 Ah (20.25 Ah L^{-1}), exhibited significantly lower capacity utilization of approximately 4.39%, based on an initial discharge capacity of 0.53 Ah (0.88 Ah L^{-1}) under identical cycling conditions. This capacity utilization reflects a discharge from a theoretically charged capacity of 8.29%, resulting in a gap of approximately 3.9% due to early inefficiencies. The reduced capacity utilization potentially limits proton conversion and results in less pronounced pH shifts. Consequently, the weaker alkalinity gradient may inadequately enhance electrode kinetics, negatively impacting overall performance. The Fe deposited gradually declined to 1.76 g in the 300 mL experiment. At the same time, volumetric utilization decreased to 1.87%, indicating a diminished electrode pore space usage despite identical charge input.

Additionally, the limited charge passed per cycle may not effectively promote iron deposition, affecting electrode kinetics and energy efficiency. The relatively low-capacity utilization in 300 mL electrolyte volume experiment also amplifies parasitic losses, such as hydrogen evolution, ultimately limiting energy conversion efficiency. Throughout the testing period, the discharge capacity and coulombic efficiency (CE) of all electrolyte volumes increased by approximately 15–20% up to the 25th cycle (see Table 1), underscoring the beneficial role of the integrated recombination cell in mitigating hydrogen-related losses. The recombination cell facilitates hydrogen removal by converting H_2 (produced *via* HER) into Fe^{2+} *via* the reduction of Fe^{3+},indirectly moderating the pH increase in the system. The absence of precipitation in any of the tests further supports the effectiveness of the recombination cell. However, irreversible hydrogen loss due to the open laboratory setup and potential iron loss from electrode adhesion issues cannot be entirely ruled out. The discharge energy graph in Fig. 5(a) showed stabilization after the initial cycles across all electrolyte volumes. Both the discharge energy and energy efficiency (EE) data in Fig. 4(c) and 5(a) highlight the significant impact of capacity utilization on IRFB performance.

For instance, the 60 mL electrolyte volume experiment delivered 0.82 Wh (6.83 Wh L^{-1}) of discharge energy and achieved 62% EE at the 25th cycle (see Table 1). This performance is attributed to the effective utilization of active species and improved reaction kinetics, enhanced by pH shifts resulting from proton consumption and redistribution. Voltage efficiency (VE), as shown in Fig. 4(d), also improved by 7% over 25 cycles. The discharge energy increased rapidly from approximately 0.52 Wh (4.33 Wh L^{-1}) in the first cycle to 0.75 Wh (6.25 Wh L^{-1}) by the 10th cycle, alongside an EE increase from ~36% to 56%. This trend reflects the stabilization of the system into a higher capacity utilization regime with more favorable reaction kinetics and iron deposition. In contrast, the 300 mL electrolyte volume experiment showed a gradual rise in discharge energy from 0.33 Wh (0.55 Wh L^{-1}) to 0.51 Wh (0.85 Wh L^{-1}) by the 10th cycle, with EE improving from 20% to 40% (standard deviation ~5%).

Intermediate electrolyte volumes (100 mL, 150 mL, 200 mL) displayed moderate performance improvements, reflecting a balance between enhanced reaction kinetics and manageable diffusion limitations. For example, the 150 mL electrolyte volume experiment increased from 0.4 Wh to 0.66 Wh in discharge energy, with EE improving from 30% to 53% over 25 cycles. This intermediate performance likely represents a trade-off between higher active species concentration and mitigating extreme diffusion limitations. As shown in Fig. 4(d), VE trends for these intermediate volumes remained relatively stable during repeated cycling, suggesting reliable system behavior. Finally, Fig. 5(b) illustrates that it means CE, EE, and VE values decreased with increasing electrolyte volume at mean of 25 charge/discharge cycles. At 60 mL electrolyte volume, the IRFB achieved a CE of nearly 93%, while at 300 mL, CE dropped to approximately 82%, highlighting challenges in mass transport and electrode surface utilization in larger volumes. EE followed a similar trend, declining from 58% at 60 mL to 42% at 300 mL experiments. These results underscore the advantage of smaller electrolyte volumes in enabling higher capacity utilization within limited cycle durations, thus enhancing capacity utilization, discharge energy, and overall energy efficiency.

Influence of increasing charging durations on performance at constant maximum theoretical capacity. To understand the performance characteristics of the iron/iron redox flow battery, a series of experiments was conducted with varying charging times of 0.5, 1, 2, 4, and 8 hours, while maintaining a constant electrolyte volume of 200 mL ($Q_{theo,max}$ = 8.01 Ah, or 20.25 Ah L^{-1}) in both storage tanks. The corresponding theoretical maximum capacity utilization after each charging cycle can be achieved ranged from approximately 6.25% (for 0.5 hours) to 100% (for 8 hours), based on a constant current of 1 A (25 mA cm^{-2}).

Fig. 6(a) shows that discharge capacity consistently increases with higher charging times. At 0.5 h, the limited reaction time restricts electrochemical processes, resulting in a discharge capacity of only 0.38 Ah (0.95 Ah L^{-1}), corresponding to a capacity utilization of approximately 4.7% relative to $Q_{theo,max}$. The reduced reaction duration limits Fe^{2+} conversion and minimizes the amount of hydrogen generated at the negative electrode. Consequently, proton (H^+) conversion is expected to remain low, and it is theoretically assumed that this results in only a slight increase in pH in the negative electrolyte tank. While such a modest alkalinity shift could help maintain a stable electrochemical environment, it may also limit potential improvements in iron plating and stripping kinetics.

As the charging time increased from 0.5 h to 8 h, redox reactions became more complete, with discharge capacity rising to 5.52 Ah (13.8 Ah L^{-1}), corresponding to a capacity utilization of approximately 68% by the 25th charge/discharge cycle. The remaining 32% (2.58 Ah) may not have been utilized

 © 2025 The Author(s). Published by the Royal Society of Chemistry

Open Access Article. Published on 14 July 2025. Downloaded on 4/18/2026 5:06:11 AM.
This article is licensed under a Creative Commons Attribution 3.0 Unported Licence.

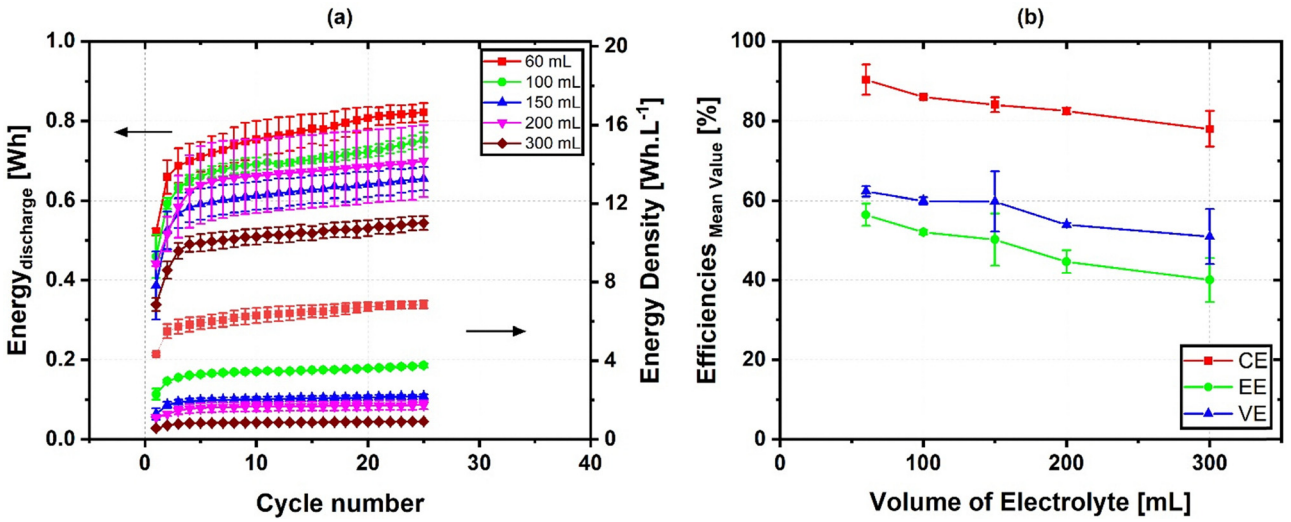

Fig. 5 Performance metrics of IRFBs with varied electrolyte volumes with constant 1-hour charge/discharge. (a) discharge energy & specific discharge energy *vs.* cycles, (b) mean efficiency values with standard deviations *vs.* electrolyte volume. The experiments were conducted at room temperature with a charge/discharge time of 1 hour at varied electrolyte volumes. The electrolyte composition was 1.5 M $FeCl_2$, 2 M NH_4Cl, and 0.2 M HCl. The charge/discharge process employed a rest period of 5 minutes and a current density of 25 mA cm^{-2}. All experiments are the mean of two experiments with standard deviations.

due to side reactions such as hydrogen evolution, incomplete iron plating/stripping, and increased protons or iron species crossover across the membrane during extended charging. Furthermore, degradation of the carbon-based negative electrode material during prolonged 8 h charge/discharge experiment was observed. Particulate residues of carbon fabric were detected in the negative tank after cycling, as confirmed by magnetic stirring and visual inspection, ruling out iron precipitation. This degradation is likely associated with extended charge durations that promote excessive hydrogen evolution reaction (HER), leading to persistent gas bubble formation and localized mechanical stress on the electrode surface. Similar degradation pathways have been reported in vanadium redox flow battery studies, where sustained HER activity induced structural damage and reduced electrode performance.[35]

Additionally, iron deposition increased with charge duration, rising from 0.804 g at 0.5 hours to 15.2 g at 8 hours (Table 2). This trend led to a significant rise in volumetric electrode utilization from 0.85% to 16.10%, reinforcing the direct correlation between the amount of charge applied and iron accumulation in the spatial matrix. These findings illustrate that an increase in charging time enhances discharge performance and facilitates greater filling of pore spaces, which becomes a crucial factor for the long-term stability of materials and cells. This trend is similarly reflected in the CE data (Fig. 6(b)). At 0.5 h, CE remains limited to over 25 cycles due to low charge carrier conversion and a relatively higher proportion of parasitic side reactions. As charging time increases toward 8 h, CE improves due to more efficient redox processes and a reduced impact from hydrogen evolution. Longer charging durations also promote potential stronger pH shifts in the negative tank, thereby enhancing iron deposition kinetics. However, proton back-diffusion from the positive to the negative half-cell remains a possible counter-effect, and the influence of such processes is expected to be dependent on current density. Fig. 6(c) and (d) illustrate a significant improvement in both energy efficiency (EE) and voltage efficiency (VE) as charging time increases. For instance, at 0.5 h, EE averaged 38.7%, while at 8 h, EE improved to 53.32%. At 2 h, EE and VE reached approximately 43.22% and 57.84%, respectively, with a capacity density of 3.96 Ah L^{-1} averaged over 25 charge/discharge cycles. At 4 h, the EE increased to approximately 58.13%, and VE improved to 62.45%. This corresponded to a discharge capacity of 3.50 Ah (8.75 Ah L^{-1}) and a discharge energy of 3.08 Wh (7.70 Wh L^{-1}) after 25 cycles. These results indicate significant performance gains at intermediate charging times (2–4 h). Fig. 7(a) shows that discharge energy increases as the charging time increases. Starting at 0.5 h, discharge energy is relatively low at 0.3 Wh (0.75 Wh L^{-1}), but it peaks at 3.94 Wh (9.85 Wh L^{-1}) during the 25th cycle at 8 h (see Table 2). This data confirms that longer charging durations allow for more efficient energy conversion. Fig. 7(b) reinforces the trend of enhanced mean efficiency and capacity utilization across extended charging times. As shown in Fig. 7(b), the Q/Q_0 trend rises steeply from 0.5 h to 4 h, indicating a sharp improvement in capacity recovery within this range. Beyond this point, the curve begins to plateau, reflecting diminishing gains in discharge capacity due to increased potential losses from crossover, electrode polarization, and incomplete redox conversion at high-capacity utilization conditions.

In summary, the findings indicate that both electrolyte volume and charging time significantly impact capacity utilization and overall, Fe/RFB performance. Under a constant one-hour cycling protocol, smaller electrolyte volumes particularly the 60 mL system (20.25 Ah L^{-1}) charged to 41% theoretical capacity utilization achieved the highest capacity utilization

Open Access Article. Published on 14 July 2025. Downloaded on 4/18/2026 5:06:11 AM.
This article is licensed under a Creative Commons Attribution 3.0 Unported Licence.

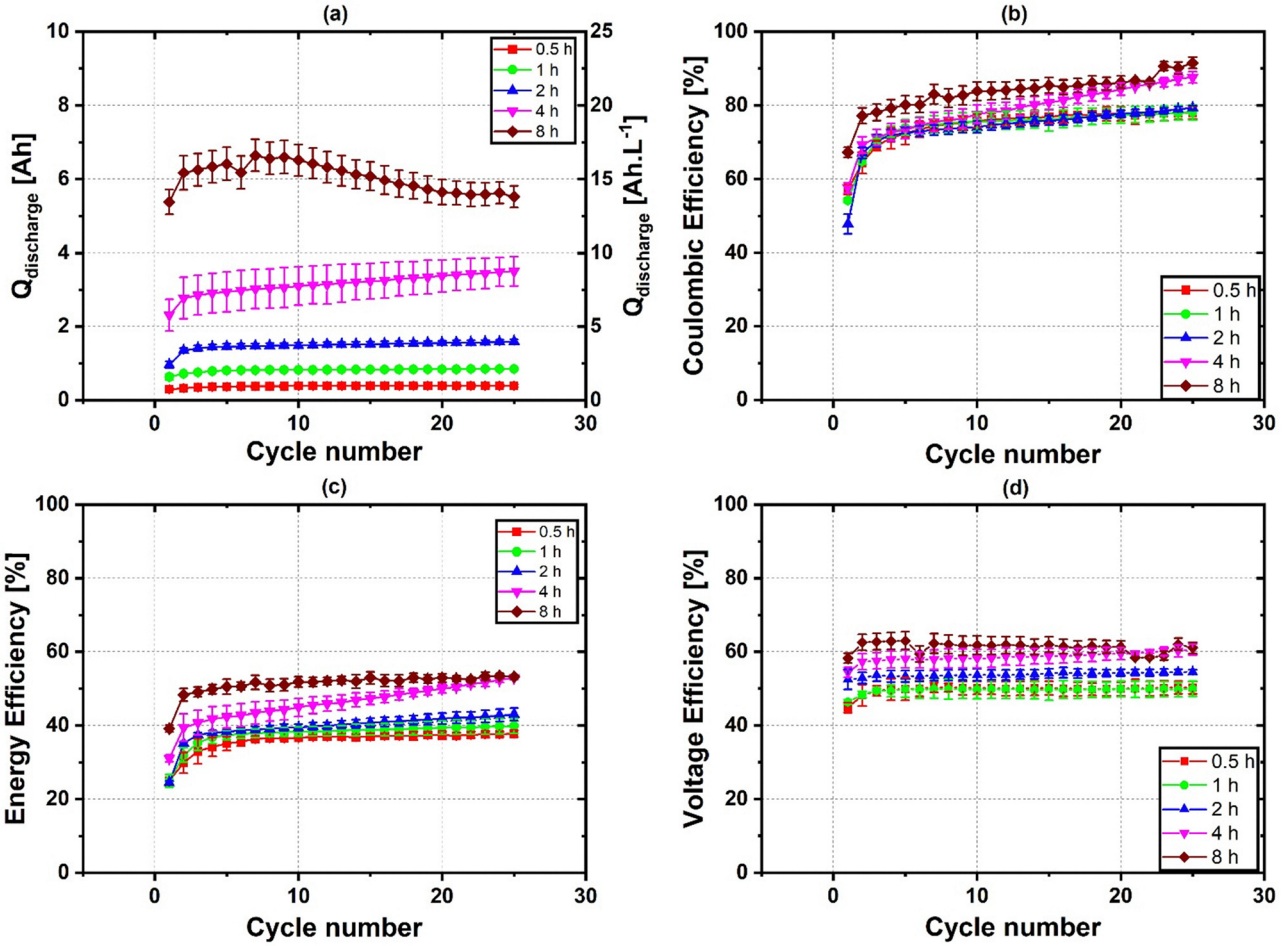

Fig. 6 Performance metrics of IRFBs with varied charge/discharge times with constant electrolyte volume. (a) discharge capacity & specific discharge capacity *vs.* cycles, (b) coulombic efficiency *vs.* cycles, (c) energy efficiency *vs.* cycles, (d) voltage efficiency *vs.* cycles. The experiments were conducted at room temperature with electrolyte volume of 200 : 200 mL (theoretical capacity - 8 Ah) at varied charge/discharge times with CC method. The electrolyte composition was 1.5 M $FeCl_2$, 2 M NH_4Cl, and 0.2 M HCl. The charge/discharge process employed a rest period of 5 minutes and a current density of 25 mA cm^{-2}. All experiments are the mean of two experiments with standard deviations.

(39.83%), capacity density (7.83 Ah L^{-1}), and energy density (6.83 Wh L^{-1}). This was accompanied by the highest Fe mass deposition (1.94 g) and volumetric electrode utilization (2.05%), reflecting more effective engagement of the electrode pore space. In contrast, the 300 mL experiment, despite having a higher theoretical capacity, showed reduced capacity utilization (6.88%), Fe deposition (1.76 g), and volumetric electrode utilization (1.87%), due to limited SOC access and dilution effects under fixed charge conditions.

When electrolyte volume was held constant (200 mL) and capacity utilization was increased through longer charge durations, the system exhibited steady gains in energy recovery and material engagement. At 4 h charging time, performance was optimized with 7.27 g of Fe deposited and 7.69% volumetric electrode utilization, balancing energy output (3.08 Wh) and efficiency (EE-58.1%, VE-62.4%). Beyond this point, Fe accumulation continued, reaching 15.2 g and 16.10% utilization at 8 h charge/discharge experiment, but with increasing risks of crossover of ions and HER. These findings emphasize the need to balance electrolyte-side capacity and electrode pore occupation to maximize energy recovery while avoiding long-term degradation.

Effect of rest time between charge–discharge cycles on iron/iron redox flow batteries performance

This section investigates the performance characteristics of the iron/iron redox flow battery (IRFB) with respect to varying rest durations between charge and discharge cycles. All experiments were executed with a constant total electrolyte volume of 400 mL (200 mL in each tank), corresponding to a maximum theoretical capacity ($Q_{theo,max}$) of 8.01 Ah (20.25 Ah L^{-1}). The charge and discharge steps were conducted for one hour, resulting in a maximum capacity utilization of approximately 12.42% relative to $Q_{theo,max}$, at a current density of 25 mA cm^{-2}. Each experimental condition regarding rest duration was repeated twice to assess statistical reliability and standard deviation.

© 2025 The Author(s). Published by the Royal Society of Chemistry

Open Access Article. Published on 14 July 2025. Downloaded on 4/18/2026 5:06:11 AM. This article is licensed under a Creative Commons Attribution 3.0 Unported Licence.

Table 2 Summary of performance metrics at the 25th cycle for iron/iron redox flow batteries operated under varied charge times (0.5–8 hours). All experiments were performed under constant current conditions (25 mA cm^{-2}) with a fixed theoretical capacity of 8.01 Ah and a 5-minute rest period between charge and discharge steps. The electrolyte volume was held constant at 200 mL with a composition of 1.5 M $FeCl_2$, 2 M NH_4Cl, and 0.2 M HCl. Tests were conducted at room temperature. Reported metrics include Fe deposited, volumetric electrode utilization, CE, EE, VE, and energy/capacity densities calculated from measured discharge performance

Charging time [h]	$Q_{max,theo}$ [%]	$Q_{discharge}$ [Ah]	$Q_{density}$ [Ah L^{-1}]	$Fe_{deposited}$ (g)	$V_{electrode\ utilization}$ (%)	$E_{density}$ [Wh L^{-1}]	CE [%]	EE [%]	VE [%]
0.5	6.25	0.38	0.95	0.804	0.85	0.75	77.15	37.60	49.68
1	12.28	0.84	2.10	1.60	1.70	1.75	77.54	39.76	49.34
2	25.36	1.58	3.96	3.30	3.49	3.20	79.31	42.54	53.77
4	50.05	3.50	8.75	7.27	7.69	7.61	87.02	52.94	58.54
8	100	5.52	13.8	15.2	16.10	9.85	91.61	53.16	61.19

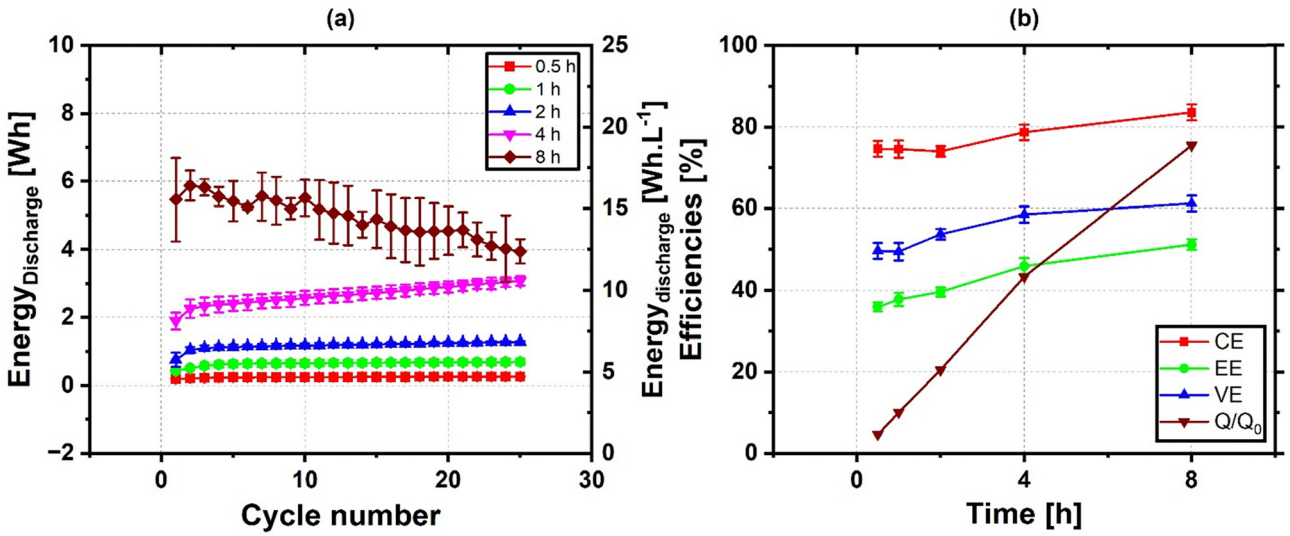

Fig. 7 Performance metrics of IRFBs with varied charge/discharge times with constant electrolyte volume. (a) Discharge energy & specific discharge energy *vs.* cycles, (b) mean efficiency values with standard deviations *vs.* electrolyte volume. The experiments were conducted at room temperature with a maximum theoretical capacity of 8.01 Ah at varied charge/discharge times. The electrolyte composition was 1.5 M $FeCl_2$, 2 M NH_4Cl, and 0.2 M HCl. The charge/discharge process employed a rest period of 5 minutes and a current density of 25 mA cm^{-2}. All experiments are the mean of two experiments with standard deviations.

Notably, a 60-minute rest interval elicited a typical performance trend. Initially, this experiment resulted in highest discharge capacity (see Fig. 8(a)) of 0.82 Ah (2.05 Ah L^{-1}), corresponding to a capacity utilization of approximately 10.2%. This phenomenon was primarily attributed to accelerated hydrogen evolution in the negative half-cell coupled with elevated coulombic efficiency during the initial cycle. However, a significant decline in discharge capacity was observed in subsequent cycles, dropping to 0.56 Ah (1.40 Ah L^{-1}) by the second cycle and stabilizing at approximately 0.76 Ah (1.90 Ah L^{-1}) by the 25th cycle. Fig. 9(a) illustrates the charge voltage profile for this case, revealing deviations from profiles observed under shorter rest conditions. For instance, while the first and second cycles achieved a charge voltage of 1.41 V over 3600 seconds, subsequent cycles exhibited prolonged open-circuit voltage (OCV) plateaus, particularly during the 3rd, 6th, and 9th cycles, suggesting potential membrane instability or internal short-circuiting. Such abnormalities likely inhibited voltage recovery and curtailed energy throughput, contributing to prolonged low-voltage phases and inefficiencies during the charging phase.

These phenomena led to diminished voltage efficiency (VE) and energy efficiency (EE), in addition to a reduction in energy density (Wh L^{-1}), for 60 minutes rest periods between charge/discharge cycles. As depicted in Fig. 8(c) and (d), both VE and EE remained systematically lower for the 60-minute rest duration, although transient improvements were noted due to fluctuations in charge voltage. The extended low-voltage durations, persisting for up to 2200 seconds in cycles 9 through 25 (Fig. 9(a)), further underscore the detrimental impact of prolonged rest durations on energy performance. In contrast, the discharge voltage profiles (not shown) demonstrated relative stability across all rest intervals, indicating minimal influence of post-charge resting on discharge behaviors. Nonetheless, the overall performance of the 60-minute resting condition was compromised, potentially due to membrane instability, increased internal resistance, or hydrogen accumulation.

Open Access Article. Published on 14 July 2025. Downloaded on 4/18/2026 5:06:11 AM.
This article is licensed under a Creative Commons Attribution 3.0 Unported Licence.

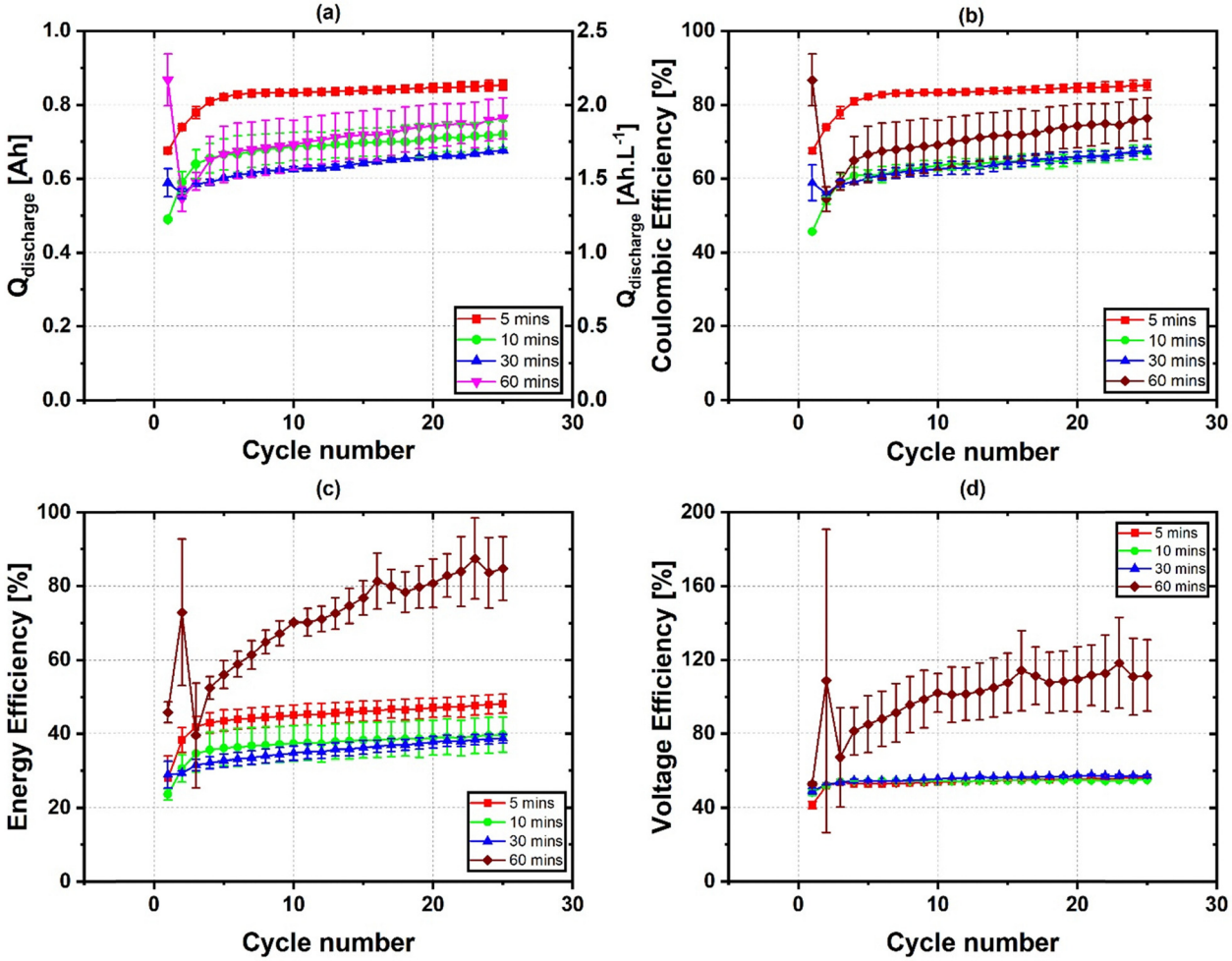

Fig. 8 Performance metrics of IRFBs with varied rest times with constant 1-hour charge/discharge and constant electrolyte volume. (a) discharge capacity & specific discharge capacity *vs.* cycles, (b) coulombic efficiency *vs.* cycles, (c) energy efficiency *vs.* cycles, (d) voltage efficiency *vs.* cycles. The experiments were conducted at room temperature with a charge/discharge of maximum 1 hour at varied rest times. The electrolyte composition was 1.5 M $FeCl_2$, 2 M NH_4Cl, and 0.2 M HCl. The electrolyte volume for all experiments is 200 : 200 mL (Maximum theoretical capacity - 8.01 Ah) and a current density of 25 mA cm^{-2}. All varied rest time values are the mean of three experiments with standard deviations.

Shorter rest intervals of 5, 10, and 30 minutes displayed comparatively stable electrochemical performance. Fig. 8(a) and (b) reveal a steady but less pronounced decline in discharge capacity and Coulombic efficiency over 25 cycles compared to the 60-minute interval. Initial discharge capacities were recorded at 0.67 Ah (1.68 Ah L^{-1}) for the 5-minute case, 0.49 Ah (1.23 Ah L^{-1}) for the 10-minute case, and 0.59 Ah (1.48 Ah L^{-1}) for the 30-minute case. These values exhibited a gradual increase of capacity utilization throughout the cycling process, likely attributable to pH evolution effects that enhanced redox reaction kinetics. By the 25th cycle, all shorter rest conditions exhibited improved discharge capacity and coulombic efficiency, with the 5-minute rest interval demonstrating better performance, potential benefiting from reduced hydrogen accumulation, minimized polarization, and suppressed self-discharge, thereby resulting in more stable overall performance. Fig. 8(c) and (d) corroborate that VE and EE progressively improved across the 25 cycles for the 5-minute and 10-minute rest conditions. Specifically, the 5-minute rest case achieved approximately 50.15% EE and 59.15% VE at the 25th cycle, whereas the 10-minute condition achieved 41.15% EE and 58.54% VE. These findings suggest that shorter rest intervals may mitigate polarization and membrane blockages. The 30-minute case also demonstrated moderate improvements, concluding 45.25% EE and 55.24% VE, albeit slightly lower than those observed for the shorter intervals while maintaining performance consistency.

In conclusion, these findings elucidate the critical role of rest periods in influencing the overall performance of the cell, emphasizing the necessity to optimize these intervals to balance capacity retention and operational efficiency. Data presented in Table 3 and Fig. 9(b) indicate that the 60-minute rest period exhibits unusually high values for energy and voltage efficiencies, which may imply potential experimental uncertainties warranting further investigation by giving 60 min rest time only after full charge/discharge cycle. The prolonged rest

© 2025 The Author(s). Published by the Royal Society of Chemistry

Open Access Article. Published on 14 July 2025. Downloaded on 4/18/2026 5:06:11 AM.
This article is licensed under a Creative Commons Attribution 3.0 Unported Licence.

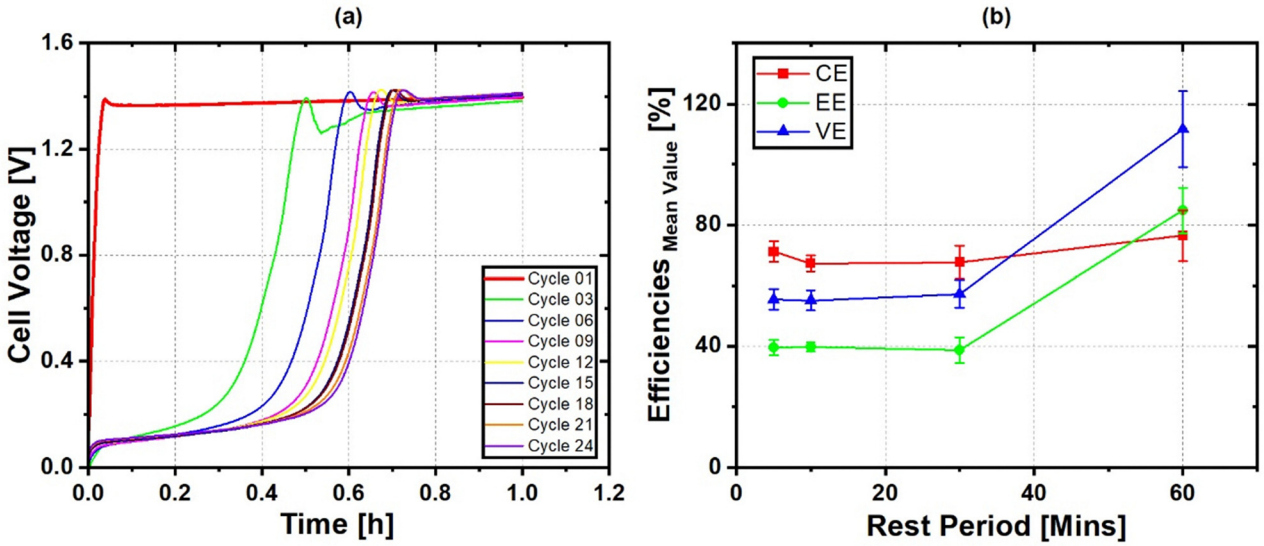

Fig. 9 Performance metrics of IRFBs with varied rest times with constant 1-hour charge/discharge and constant electrolyte volume. (a) charge cell voltage *vs.* time curves of 60 min rest time experiment, (b) mean efficiencies *vs.* cycles; the experiments were conducted at room temperature with a charge/discharge time of 1 hour at varied rest times. The electrolyte composition was 1.5 M $FeCl_2$, 2 M NH_4Cl, and 0.2 M HCl. The electrolyte volume for all experiments is 200 : 200 mL and a current density of 25 mA cm^{-2}. All varied rest time values are the mean of three experiments with standard deviations.

Table 3 Performance metrics at the 25th cycle for iron/iron redox flow batteries with varied rest times (5–60 min) under constant current conditions. The experiments were conducted with a theoretical capacity of 8.01 Ah (20.25 Ah L^{-1}), a max theoretical capacity utilization was aimed until 12.4%, with a 25-mA cm^{-2} current density. The electrolyte composition was 1.5 M $FeCl_2$, 2 M NH_4Cl, and 0.2 M HCl, and experiments were performed at room temperature

Rest Time [min]	$Q_{theoretical}$ [Ah]	$Q_{discharge}$ [Ah]	$Q_{utilized}$ [%]	Capacity density [Ah L^{-1}]	$E_{discharge}$ [Wh]	Energy density [Wh L^{-1}]	CE [%]	EE [%]	VE [%]
5	8.01	0.65	8.12	1.63	0.64	1.60	82.1	48.5	55.5
10	8.01	0.47	5.87	1.18	0.52	1.30	68.7	39.3	54.4
30	8.01	0.56	6.99	1.40	0.59	1.48	69.2	38.2	56.1
60	8.01	0.76	9.49	1.90	0.82	2.05	78.1	83.4	112.3

durations, particularly the 60-minute interval, introduce significant inefficiencies, likely stemming from a suspected internal short circuit within the cell, which may contribute to membrane blockages and increased ohmic resistance, ultimately impairing charge performance and overall battery efficiency. In contrast, shorter rest durations until 30 min yielded enhanced performance metrics across the board.

Effect of charge cutoff voltages on iron/iron redox flow batteries performance using constant current method

A series of galvanostatic charge–discharge experiments were conducted to investigate the influence of charge cutoff voltage on the performance of the iron/iron redox flow batteries. Iron/iron redox flow batteries were cycled with varying charge cutoff voltages, ranging from 1.55 V to 1.9 V, while maintaining a constant discharge cutoff voltage of 0 V in discharging phase, current density of 25 mA cm^{-2}, maximum theoretical capacity of 2.43 Ah (electrolyte volume of 60 mL on both electrolyte tanks, 20.25 Ah L^{-1}) and rest time of 5 minutes between charge/discharge cycles. In Fig. 10(a–d), the discharge capacity, coulombic efficiency (CE), voltage efficiency (VE), and energy efficiency (EE) were analysed as a function of cycle number to assess the impact of charge cutoff voltage on capacity retention and overall battery performance.

When examining iron/iron redox flow batteries, an interesting trend emerged while adjusting the charge cutoff voltage. Increasing the cut-off voltage from 1.5 V to 1.9 V decreases energy efficiency (EE) while simultaneously discharge capacity increased. Conversely, lowering the charge cutoff voltage from 1.9 V to 1.5 V improved energy efficiency, reducing the discharge capacity. Higher charge cutoff voltages enhanced active material utilization in batteries, increasing capacity utilization, though this might result in lower efficiency and chances of crossover of electrolytes. The increased charge cutoff voltage results in more hydrogen evolution at the negative electrode, leading to proton conversion and an potential increase in pH within the negative electrolyte tank. This alkalization influences side reactions and modifies the electrochemical environment, impacting the long-term stability of iron plating and stripping kinetics. Based on these insights, targeting a charge

Open Access Article. Published on 14 July 2025. Downloaded on 4/18/2026 5:06:11 AM.
This article is licensed under a Creative Commons Attribution 3.0 Unported Licence.

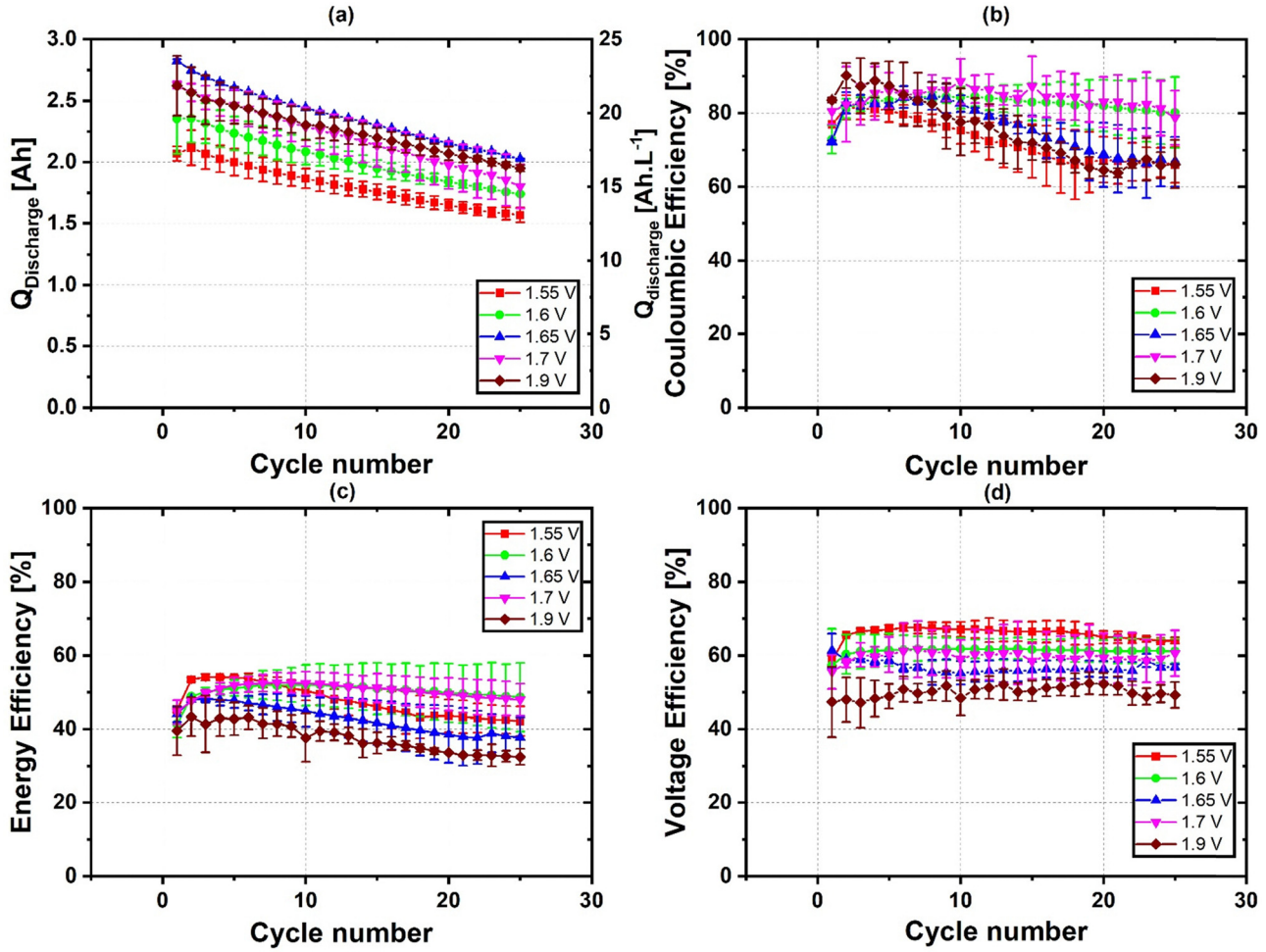

Fig. 10 Performance metrics of IRFBs with varied charge cut-off voltages with constant current method. (a) discharge capacity & specific discharge capacity *vs*. cycles, (b) coulombic efficiency *vs*. cycles, (c) energy efficiency *vs*. cycles, (d) voltage efficiency *vs*. cycles. The experiments were conducted at room temperature with an electrolyte volume of 60 : 60 mL (maximum theoretical capacity - 2.43 Ah) at varied charge cutoff voltages and discharge cutoff voltage of 0 V. The electrolyte composition was 1.5 M $FeCl_2$, 2 M NH_4Cl, and 0.2 M HCl. The charge/discharge process employed a rest period of 5 minutes and a current density of 25 mA cm^{-2}. All experiments are the mean of two experiments with standard deviations.

cutoff voltage between 1.55 V and 1.65 V could optimize energy efficiency. However, if the aim is to maximize discharge capacity, a range of 1.7 V to 1.9 V may be more advantageous.

Initially, in Fig. 10(a), a clear hierarchy in discharge capacity was observed, with the highest values achieved at the highest cutoff voltages of 1.9 V and 1.7 V, followed by 1.65 V, 1.6 V, and 1.55 V. For the 1.9 V and 1.7 V cutoff conditions, the initial discharge capacities approach the theoretical limit of 2.43 Ah. In contrast, lower cutoff voltages exhibit conservative energy storage due to reduced active material utilization. A moderately high initial discharge capacity was observed at the intermediate voltages of 1.65 V and 1.6 V. The rate of capacity decay is less noticeable than at 1.9 V, indicating a balance between maximizing energy storage and minimizing degradation. This balance results in a more gradual reduction in discharge capacity over the charge/discharge cycle. The stability observed at these intermediate cutoff voltages may reflect a lower rate of hydrogen evolution, contributing to better long-term capacity retention. At these voltages, the moderate pH shift stabilizes the electrolyte composition, preventing excessive hydrogen evolution while maintaining favorable iron plating and stripping kinetics. This controlled environment supports long-term cycling stability and improved energy recovery.

At the lowest cutoff voltage of 1.55 V, the initial discharge capacity is the lowest due to hydrogen evolution during charging. However, this low cutoff voltage demonstrates the most stable cycling behaviour, with the least capacity fading across 25 cycles. The reduced likelihood of side reactions at lower charge cut-off voltage parameter accounts for this stability and reduced hydrogen evolution at the negative electrode due to the limited extent of Fe^{2+} oxidation. Consequently, the recombination cell has a lower demand for hydrogen removal and Fe reduction, minimizing its overall impact on the electrolyte composition. With less proton conversion from hydrogen evolution, the pH increase in the negative electrolyte tank is also likely less pronounced compared to higher charge cut-off voltages. This stability results in significantly higher energy capacity. The lower charge cutoff voltage restricts hydrogen

© 2025 The Author(s). Published by the Royal Society of Chemistry

Open Access Article. Published on 14 July 2025. Downloaded on 4/18/2026 5:06:11 AM. This article is licensed under a Creative Commons Attribution 3.0 Unported Licence.

evolution, leading to minimal proton conversion and a slower pH shift. This stabilization reduces parasitic side reactions, contributing to the observed steady performance and prolonged cycle life. This suggests that operating at this voltage may be more suitable for applications where energy density is prioritized over cycle life.

Coulombic efficiency (CE), as shown in Fig. 10(b), provides additional insight into the battery's performance under varying charge cutoff voltages. Across all charge cutoff voltages, CE initially increased over the first few charge/discharge cycles as the battery stabilized. High charge cutoff voltages, such as 1.9 V, show high initial CE values due to low pH, which resembles higher hydrogen evolution but exhibits noticeable declines as charge/discharge cycling continues. This decrease in CE can be attributed to side reactions that consume active material, particularly at higher charge cut-off voltages, disrupting the electrolyte balance and leading to efficiency losses. The decline in CE for the 1.9 V charge cut-off condition was accompanied by significant variability, as indicated by larger standard deviations, suggesting intermittent side reactions, such as hydrogen evolution and cross over, which occur sporadically and impact the battery's efficiency in recovering stored charge. This variability at 1.9 V highlights the challenges associated with high cutoff voltages, including the need for more complex control systems to manage these side reactions.

In contrast, intermediate charge cutoff voltages of 1.6 V and 1.65 V demonstrate more stable CE values with lower variability over cycles. This stability implies a balanced reaction environment with lower parasitic reactions, allowing for more consistent charge recovery. Additionally, the extent of proton diffusion from the positive half-cell to the negative half-cell varies with charge cutoff voltage. At higher voltages, increased proton conversion from hydrogen evolution can drive diffusion back into the negative half-cell, influencing overall pH dynamics and reaction kinetics and further impacting battery efficiency and stability over extended cycling. The lowest charge cutoff voltage of 1.55 V maintains the most stable CE across cycles, with minimal deviations. However, the overall CE at 1.55 V is slightly lower than at intermediate voltages due to limited active material utilization, which restricts the charge transfer efficiency.

Voltage efficiency (VE) and energy efficiency (EE) trends are shown in Fig. 10(c) and (d), respectively. Voltage efficiency followed a decreasing trend with increasing charge cutoff voltage, indicating increased polarization losses and higher overpotential. Similarly, energy efficiency declines at higher charge cutoff voltages due to a combination of decreased voltage efficiency and additional parasitic losses from side reactions. Lower charge cutoff voltages, such as 1.55 V and 1.6 V, exhibit higher energy efficiency values as they minimize hydrogen evolution and side reactions, preserving overall system efficiency over extended cycling.

The reductions in voltage efficiency (VE) and energy efficiency (EE) at elevated charge cutoff voltages can be attributed to several sources of overpotential that arise during the charging process. As the system approaches 1.9 V, activation overpotential increases due to the slower kinetics of the iron redox reactions at the electrode surface. This leads to increased energy input requirements and a decline in VE. These effects are compounded by parasitic side reactions such as water electrolysis, which becomes more likely as the cell approaches 1.9 V. This reaction generates hydrogen at the negative electrode, leading to hydrogen evolution, simultaneously resulting in proton generation at the positive electrode, causing acidification. These shifts disrupt the electrolyte balance and lower Coulombic efficiency (CE). The irreversible nature of these reactions contributes to energy losses that do not translate into useful charge storage. As energy efficiency (EE) is a product of CE and voltage efficiency (VE), this chain of overpotentials and side reactions explains the substantial decline in EE at elevated cutoff voltages. Studies on vanadium redox flow batteries have similarly demonstrated that elevated upper voltage limits significantly reduce discharge capacity and voltage efficiency, with increased overpotentials contributing to cell degradation. The results suggest that intermediate charge cutoff voltages balance maximizing both VE and EE while maintaining stable long-term cycling behaviour.[36]

In summary, the charge cutoff voltages significantly impact the overall performance of the iron/iron RFBs. High cutoff voltages, such as 1.9 V, maximize the initial discharge capacity but lead to rapid capacity fading and reduced efficiencies due to side reactions, particularly hydrogen evolution. Intermediate voltages of 1.65 V and 1.6 V offer a balanced approach, achieving moderately high initial capacities, stable coulombic efficiency, and higher energy and voltage efficiencies, suggesting minimized side reactions and improved stability over multiple cycles. The lowest cutoff voltage, 1.55 V, provides the most stable cycling performance with consistent coulombic and high energy efficiency values, though at the cost of lower capacity and slightly reduced voltage efficiency. These findings indicate that while higher cutoff voltages can enhance initial energy storage, intermediate cutoff voltages provide the best long-term balance between capacity retention and efficiency, making them more suitable for practical applications where performance and longevity are essential.

Effect of discharge cutoff voltages on iron/iron redox flow batteries performance using constant current method

The systematic evaluation of the charge/discharge cycling performance of the iron/iron RFBs was conducted over 25 cycles at varying discharge cutoff voltages: 0.6 V, 0.4 V, 0.2 V, 0.1 V, and 0 V while maintaining a constant charge cutoff voltage of 1.9 V in charging phase, current density of 25 mA cm^{-2}, maximum theoretical capacity of 2.43 Ah (20.25 Ah L^{-1}) and rest time of 5 minutes between charge/discharge cycles. This setup allowed for a systematic evaluation of battery performance across varying discharge cutoff conditions.

As the discharge cutoff voltage increased from 0.2 V to 0.6 V, a notable improvement in energy efficiency (EE) was observed, accompanied by a reduction in discharge capacity. This can be attributed to the restricted depth of discharge, which minimizes energy losses from side reactions, including hydrogen

Open Access Article. Published on 14 July 2025. Downloaded on 4/18/2026 5:06:11 AM.
This article is licensed under a Creative Commons Attribution 3.0 Unported Licence.

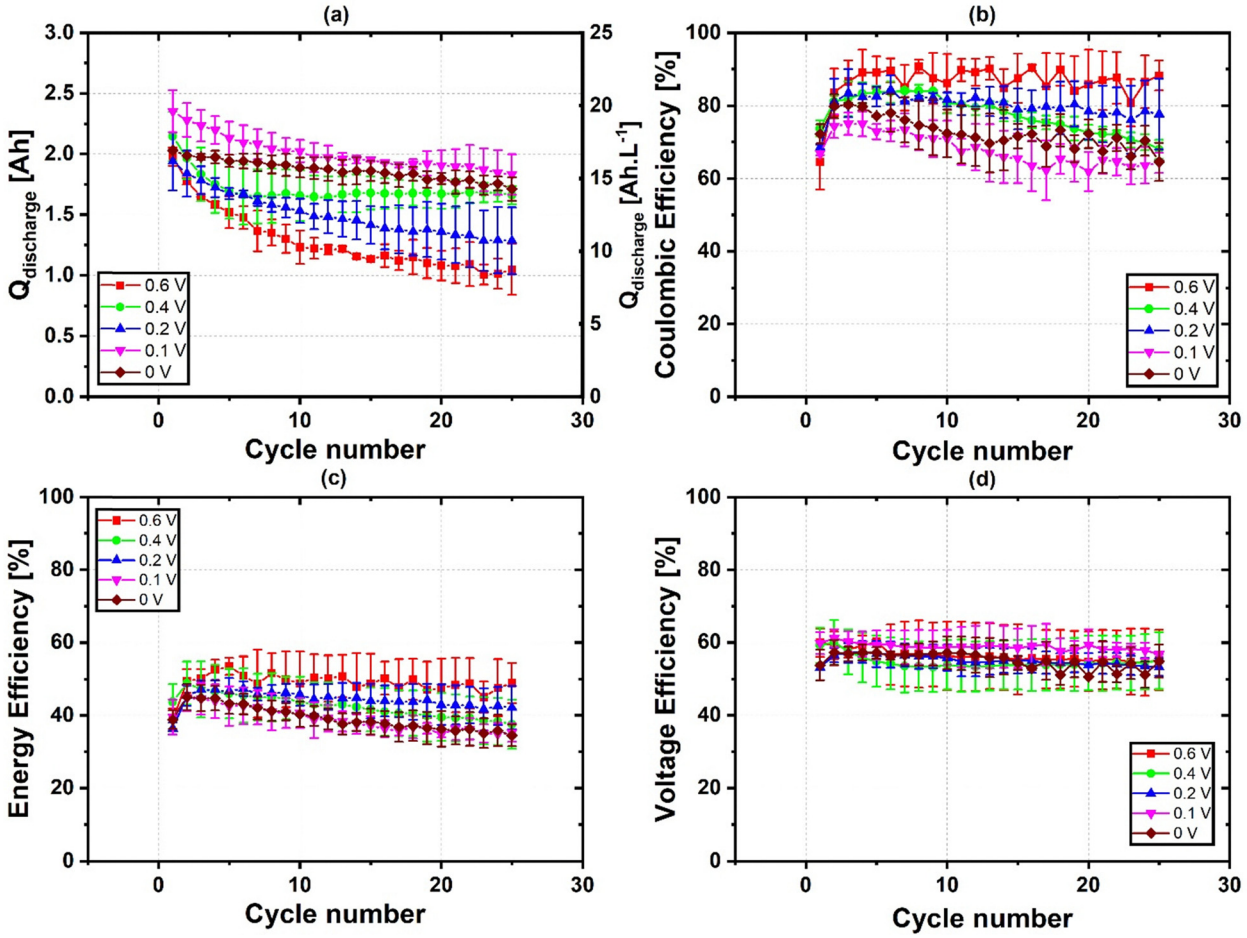

Fig. 11 Performance metrics of IRFBs with varied discharge cut-off voltages with constant current method. (a) discharge & specific discharge capacity capacity *vs*. cycles, (b) coulombic efficiency *vs*. cycles, (c) energy efficiency *vs*. cycles, (d) voltage efficiency *vs*. cycles. The experiments were conducted at room temperature with an electrolyte volume of 60 : 60 mL [maximum theoretical capacity – 2.43 Ah] at varied discharge cutoff voltages and charge cutoff voltage of 1.9 V. The electrolyte composition was 1.5 M $FeCl_2$, 2 M NH_4Cl, and 0.2 M HCl. The charge/discharge process employed a rest period of 5 minutes and a current density of 25 mA cm^{-2}. All experiments are the mean of two experiments with standard deviations.

evolution, and limits pH fluctuations in the electrolyte. Conversely, lower cutoff voltages (*e.g.*, 0.2 V to 0 V) enable greater depth of discharge and higher capacity, but at the expense of energy efficiency due to intensified parasitic reactions such as hydrogen evolution and ion crossover.

Fig. 11(a) illustrates that lower discharge cutoff voltages allowed greater depths of discharge and correspondingly higher discharge capacities. Specifically, cutoff voltages of 0.2 V, 0.1 V, and 0 V achieved the highest discharge capacities over 25 cycles, as these voltages enabled more complete conversion of iron ions. However, significant capacity fading was observed across all cutoff voltages over repeated cycles, consistent with existing literature attributing capacity loss in iron flow batteries to active material crossover and irreversible side reactions, such as the formation of insoluble iron oxides in acidic conditions.[37] During the initial 10 cycles, higher discharge cutoff voltages (0.6 V and 0.4 V) exhibited more stable, albeit lower, capacity levels. The limited depth of discharge at these voltages helped preserve active material but restricted overall capacity output. Over 25 cycles, the rate of capacity decline was more gradual at higher discharge cutoff voltages, as the less intense discharges contributed to reduced material degradation.

Fig. 11(b) illustrates that coulombic efficiency stabilized after the first few cycles, with higher values observed at higher discharge cutoff voltages, particularly at 0.6 V, where CE reached approximately 90% and remained relatively constant. This trend aligns with studies on IRFBs, which indicate that shallower depths of discharge reduce side reactions, such as hydrogen evolution, thereby enhancing CE.[19] Conversely, lower discharge cutoff voltages were associated with moderate declines in CE over time, especially for the 0.1 V and 0 V cutoffs, where CE stabilized around 70–81%. These lower cutoff voltages permit deeper discharges, increasing the risk of side reactions and iron ion crossover, leading to coulombic losses and reduced efficiency. Periodic fluctuations in CE across all discharge cutoff voltages may reflect transient changes in electrode kinetics and electrolyte composition as Fe^{2+} and Fe^{3+} ions re-equilibrate during charge–discharge cycling, a phenomenon commonly reported in similar iron-based systems.[19,29] In Fig. 11(c), energy efficiency exhibited a parallel

© 2025 The Author(s). Published by the Royal Society of Chemistry

Open Access Article. Published on 14 July 2025. Downloaded on 4/18/2026 5:06:11 AM. This article is licensed under a Creative Commons Attribution 3.0 Unported Licence.

trend to coulombic efficiency, with higher discharge cutoff voltages yielding slightly improved EE values that stabilized around 55–60% for the 0.6 V cutoff after the initial cycles. The early increases in EE over the first five cycles were likely due to the conditioning of the electrode surface and stabilization of the Fe^{2+}/Fe^{3+} and Fe/Fe^{2+} redox reactions, as observed in the early-cycle behavior of iron-based flow batteries. The energy efficiency (EE) consistently remained lower at reduced cutoff voltages, primarily due to a decrease in coulombic efficiency (CE) rather than any significant variation in voltage efficiency (VE). Since VE values remained nearly identical across cycles and cutoff voltages (as also confirmed by the relation EE = CE × VE), the lower EE at reduced cutoff voltages likely stems from increased parasitic reactions such as hydrogen evolution and higher ion crossover. By cycle 10, EE at these lower cutoff conditions had stabilized around 45–50%.

The voltage efficiency (VE) graph in Fig. 11(d) exhibited a consistent pattern across all discharge cutoff voltages, remaining in the range of 58% to 62% over 25 cycles. Although VE showed minimal variation, slight differences attributed to standard deviations were observed. This consistency indicates that discharge cutoff voltages have a limited influence on VE, as polarization and concentration gradients near the electrode surface remained largely stable, regardless of the cutoff voltage. This decoupling of EE from VE reinforces the conclusion that mitigating coulombic inefficiencies primarily due to parasitic hydrogen evolution is crucial to maintaining high energy efficiency in IRFBs.

In summary, the performance of iron/iron redox flow batteries is significantly influenced by both charge and discharge cutoff voltages. For charge cutoff voltages, increasing the voltage from 1.5 V to 1.9 V enhances discharge capacity by improving the utilization of active materials. However, this also leads to a decrease in energy efficiency (EE) due to cumulative energy losses. Conversely, lowering the charge cutoff voltage improves EE but at the expense of capacity. An optimal balance between efficiency and capacity can be achieved by targeting a charge cutoff voltage of 1.6 V to 1.7 V for optimal energy efficiency or 1.7 V to 1.9 V for maximum discharge capacity. Regarding discharge cutoff voltages, higher values (ranging from 0.2 V to 0.6 V) improve energy efficiency, but this comes at the cost of reduced discharge capacity due to the limited depth of discharge. On the other hand, lower cutoff voltages (from 0.2 V to 0 V) maximize capacity but decrease energy efficiency because of increased parasitic reactions and ion crossover. These findings underscore the importance of carefully selecting charge and discharge cutoff voltages to align battery performance with specific application requirements.

Influence of constant current (CC) and constant current-constant voltage (CCCV) methods on cycling behaviour. To evaluate the cycling behaviour and operational stability of Fe/Fe redox flow batteries (IRFBs) under demanding conditions, experiments were conducted using a charge cutoff voltage of 1.9 V and a discharge cutoff voltage of 0 V. These extreme parameters were selected to maximize the utilization of active material, enabling the system to operate near full charge and deep discharge conditions. The tests utilized 60 mL of electrolyte per tank (120 mL total), corresponding to a theoretical capacity of 2.43 Ah (20.25 Ah L^{-1}). Two distinct charging protocols were evaluated over 25 charge/discharge cycles: Constant Current (CC) and Constant Current–Constant Voltage (CCCV). This analysis aimed to determine differences in capacity retention and efficiency performance of the IRFBs. Under the CCCV method, a constant-voltage phase was initiated once the 1.9 V limit was reached, and charging was terminated when the current dropped below 100 mA. This cutoff condition ensures that the system nears electrochemical equilibrium without excessive energy input, enabling more complete redox reactions while avoiding prolonged overpotential conditions that promote side reactions.

Fig. 12(a) and (b) illustrate the charge/discharge capacities for both CCCV and CC methods. In the CCCV protocol, the initial charge capacity reached approximately 2.8 Ah (23.33 Ah L^{-1}), while the discharge capacity was around 2.3 Ah (19.17 Ah L^{-1}), indicating high initial utilization of available capacity. Notably, the charge capacity slightly exceeded the theoretical maximum (2.43 Ah or 20.25 Ah L^{-1}) in early cycles likely due to parasitic reactions such as hydrogen evolution at higher cutoff voltages. Future studies could estimate this effect by quantifying recombination cell current and calculating the associated recoverable charge. After a period of rapid decline over the first ten cycles, discharge capacity stabilized at 1.9 Ah (15.83 Ah L^{-1}) by the 25th cycle, reflecting consistent access to a significant portion of the active material. This suggests that the CCCV protocol enables more stable cycling performance under conditions of extended charge input and high-capacity utilization.

In contrast, the CC cycling method result started with a slightly lower charge capacity (2.51 Ah or 20.83 Ah L^{-1}) and discharge capacity (1.9 Ah or 15.83 Ah L^{-1}), both of which declined more significantly over time. By the 25th cycle, the discharge capacity under CC decreased to approximately 1.5 Ah (12.5 Ah L^{-1}). The performance gap between CCCV and CC can be attributed to differences in end-of-charge behavior. The CCCV protocol, by allowing the current to taper while maintaining the voltage at 1.9 V, facilitates a more complete conversion of Fe^{2+} to Fe^{3+} in the positive half-cell and potentially efficient Fe plating in the negative half-cell without exceeding the voltage potential that favors hydrogen evolution. Conversely, the CC method terminates charging as soon as 1.9 V is reached, often before achieving full charge state. This abrupt cutoff can leave a portion of active species unconverted and may lead to sudden voltage fluctuations or uneven concentration profiles near the end of the charge. Such effects reduce charge conversion efficiency and can promote non-uniform current distribution, contributing to long-term electrode degradation.

Fig. 12(c) and (d) show the system's efficiencies over 25 cycles. In the CCCV charging method, the CE begins at approximately 79.11% during the first cycle and steadily increases to about 88.25% by the fourth cycle as the battery system stabilizes. This improvement may be attributed to the

Open Access Article. Published on 14 July 2025. Downloaded on 4/18/2026 5:06:11 AM.
This article is licensed under a Creative Commons Attribution 3.0 Unported Licence.

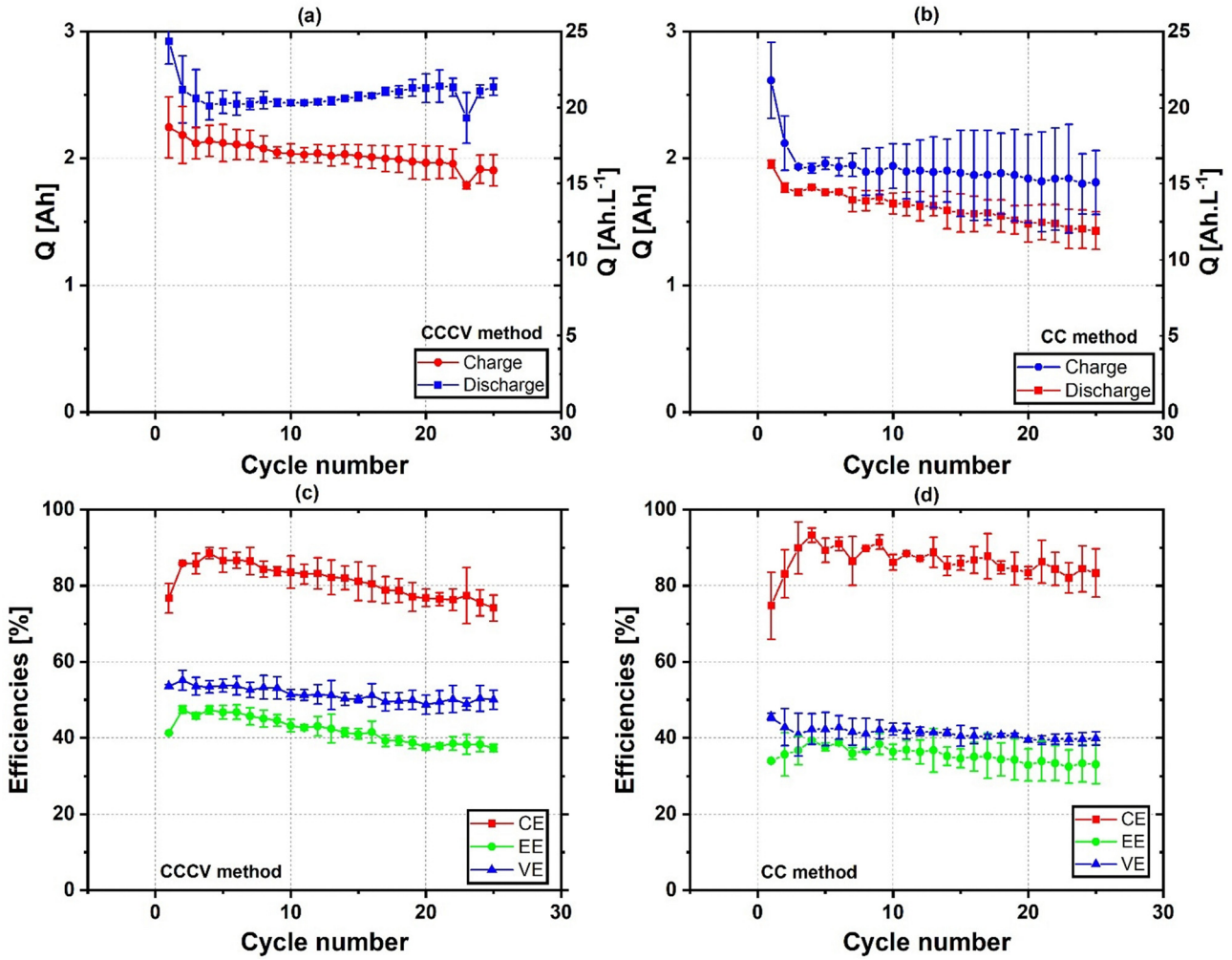

Fig. 12 Performance comparison of IRFBs with CCCV charge/discharge and constant current methods. (a) capacities & specific capacity *vs.* cycles of the CCCV method, (b) capacities *vs.* cycles of the CC method, and (c) efficiencies *vs.* cycles of the CCCV method. (d) Efficiencies *vs.* cycles of Constant Current Method. The experiments were conducted at room temperature with an electrolyte volume of 60 : 60 mL (Maximum theoretical capacity - 2.43 Ah) at charge cutoff voltage and discharge cutoff voltage of 1.9/0 V (see before). The electrolyte composition was 1.5 M $FeCl_2$, 2 M NH_4Cl, and 0.2 M HCl. The charge/discharge process employed a rest period of 5 minutes and a current density of 25 mA cm^{-2}. All experiments are the mean of two experiments with standard deviations.

constant-voltage tapering phase, which enhances charge utilization by enabling a more complete conversion of iron ions at the electrodes. However, after this peak, the CE gradually declines, reaching around 77.57% by the 25th cycle. This downward trend suggests that prolonged exposure full charge conditions during the constant-voltage phase may introduce minor parasitic reactions or limitations in reaction kinetics that accumulate over time and lower CE. In contrast, the CC charging method starts with a slightly lower CE at around 77.11%, then rises rapidly to a peak near 93.14% by the fifth cycle. This early enhancement may result from shorter charge durations and reduced time spent at high voltage conditions, which limit side reactions in early cycles. After peaking, the CE fluctuates moderately and stabilizes near 83.11% by the 25th cycle. This trend suggests that while CC initially reduces side reaction exposure, it faces limitations in achieving complete charge transfer, especially due to gradual polarization buildup and minor resistance increases that contribute to long-term efficiency losses.

Fig. 12(c) and (d) further illustrate the trends in energy efficiency (EE) and voltage efficiency (VE) over 25 cycles. In the CC method, EE starts at approximately 41.12%, rises to about 46.05% by the 10th cycle, and then declines to 39.15% by the 25th cycle. Similarly, VE begins at 56.87% and gradually drops to 49.31% by the end of the experiment. These trends indicate that while CC charging initially benefits from reduced voltage stress and shorter charge durations, it becomes increasingly impacted by internal resistance, pH drift, and incomplete redox conversion over time. In contrast, the CCCV method consistently maintains higher EE and VE values across all cycles approximately 10% higher than those of the CC method. This advantage arises from the controlled voltage plateau phase, which promotes more complete redox conversion and mitigates parasitic losses such as hydrogen evolution. Although CCCV

© 2025 The Author(s). Published by the Royal Society of Chemistry

Open Access Article. Published on 14 July 2025. Downloaded on 4/18/2026 5:06:11 AM.
This article is licensed under a Creative Commons Attribution 3.0 Unported Licence.

introduces longer charge times, it helps reduce internal polarization buildup, maintain stable reaction kinetics, and prevent abrupt pH gradients often associated with CC termination. These benefits, combined with higher capacity utilization, contribute to sustained improvements in energy and voltage efficiency.

In summary, while constant current (CC) and constant current constant voltage (CCCV) protocols are both viable for operating IRFBs, CCCV demonstrates better long-term performance through enhanced full charge conditions, improved capacity retention, and more stable electrochemical behavior. Future research could explore adaptive CCCV strategies, such as dynamic taper thresholds or real-time feedback on current and pH, to further mitigate parasitic reactions like hydrogen evolution and extend cycle life in Fe-based systems.

Impact of self-discharge on iron/iron redox flow batteries. The voltage profiles depicted in Fig. 13(a) and (b) offer valuable insights into the operational behavior of the iron/iron redox flow battery during its charging, discharging, and self-discharge periods. Grasping these phases is essential for evaluating the battery's energy storage potential. Fig. 13(a) demonstrates the charging and discharging activities at a steady current of 1 A (25 mA cm^{-2}). Fig. 12(b) concentrates on the charging phase until 1.9 V of charge cutoff voltage with a maximum theoretical capacity of 2.43 Ah, corresponding to a capacity density of 20.25 Ah L^{-1} followed by the self-discharge phase under no external load. Collectively, these voltage profiles elucidate how the battery accumulates, releases, and maintains energy.

Following the charging stage in Fig. 13(b), the battery's voltage steadily declined during self-discharge. Over the initial 20 hours, the cell sustained a relatively elevated open-circuit voltage, exhibiting only minimal reduction. This indicates that the redox-active components are stabilizing efficiently, likely aided by an incorporated recombination cell that reduces unwanted reactions and conserves the system's electrochemical potential. The self-discharge behavior is also influenced by electrolyte pH variations, which impact hydrogen evolution and overall reaction kinetics. A stable pH environment minimizes potential unintended hydrogen evolution, thereby reducing charge losses and extending the duration of self-discharge phases.

In Fig. 13(b), the self-discharge phase was categorized into three distinct stages based on changes in voltage over time. In phase 1, which endures for 30 hours, the voltage decreases from 1.25 V to 1.06 V. Conversely, phase 2 experiences a more substantial voltage decline from 1.06 V to 0.126 V over 12 hours. The self-discharge rate during phase 1 and 2, calculated using the integration of voltages between phases as end of phase 2 considered as end of discharge step, is approximately 0.0945 Ah h^{-1}, indicating a slow and stable voltage reduction over 42 hours. An increase in energy storage capacity could extend this phase even further (Table 4).

This more pronounced drop likely arises from the usage of higher energy redox states and an escalation in the crossover of active species. Subsequently, phase 3 features a more gradual voltage reduction from 0.126 V to 0.023 V across 46 hours, suggesting that energy depletion is nearing its conclusion, and that voltage is stabilizing close to zero. By the end of the 90-hour observation, the voltage had nearly approached 0 V, indicating a total loss of stored charge.

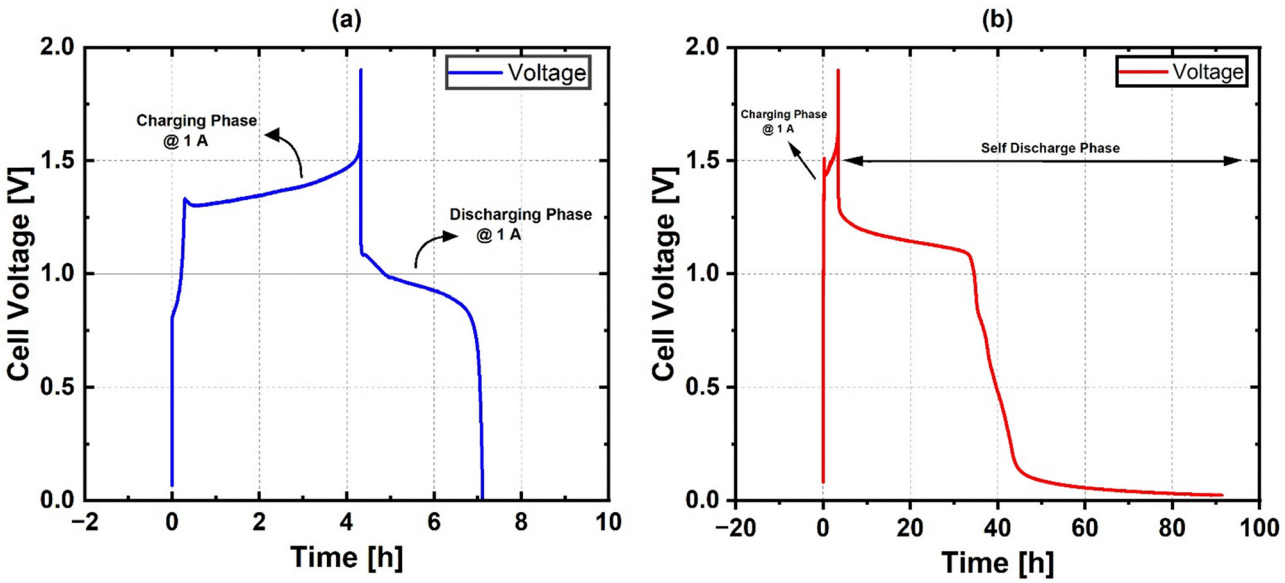

Fig. 13 Performance comparison of IRFBs self discharge parameter with charge/discharge voltage profiles. (a) Cell voltage *vs.* time, (b) cell voltage *vs.* time (self discharge profile) of constant current method. The experiments were conducted at room temperature with an electrolyte volume of 60 : 60 mL (Maximum theoretical capacity - 2.43 Ah) at charge cutoff voltage and discharge cutoff voltage of 1.9/0 V. The electrolyte composition was 1.5 M $FeCl_2$, 2 M NH_4Cl, and 0.2 M HCl. The charge/discharge process employed a rest period of 5 minutes and a current density of 25 mA cm^{-2}. The electrochemical area of the battery is 40 cm^2.

Open Access Article. Published on 14 July 2025. Downloaded on 4/18/2026 5:06:11 AM. This article is licensed under a Creative Commons Attribution 3.0 Unported Licence.

Table 4 Self-discharge characteristics of the iron/iron redox flow battery during the three identified phases. The experiments were conducted with a theoretical capacity of 2.43 Ah and a charging current of 1 A. Phase durations and voltage ranges were recorded during the self-discharge process following a complete charge. Self-discharge rates were calculated as the average slope of voltage decay for each phase by considering phase 2 end as fully discharged cell

Phase	Time (h)	Cell voltage range (V)	Self-discharge rate (Ah h^{-1})
1	30	1.25–1.06	0.0945 Ah h^{-1}
2	12	1.06–0.126	

These phases illustrate the system's challenges in preserving energy over extended durations. It was assumed that the gradual reduction in phase 1 highlights the effective role of the recombination cell in minimizing energy loss and regulating active species crossover while restraining hydrogen production. In contrast, the steep voltage declines in phase 2, followed by a slow drop in phase 3, suggest possible issues such as mass transport limitations, increased ionic crossover, and side reactions that may hinder performance. These factors decrease the number of active redox pairs and diminish the battery's ability to retain a charge.

In summary, the findings emphasize the crucial contribution of the integrated recombination cell in sustaining voltage levels and reducing self-discharge in the iron/iron redox flow battery. Nonetheless, the sharp voltage decreases noted in the later stages highlight areas requiring enhancement. Tackling these challenges could render iron-based redox flow batteries more viable for long-term energy storage.

Preliminary insights of operational parameters influencing self-discharge in iron/iron RFBs. The impact of several critical operational parameters including electrolyte volume, charge and discharge durations, rest intervals, cutoff voltages, and cycling protocols (constant current constant voltage, CCCV, *versus* constant current, CC) on the self-discharge behaviour of an all-iron redox flow battery (IRFB) system was examined with preliminary data. Initial experiments with iron/iron redox flow battery utilized a 60 mL electrolyte volume in both electrolyte tanks, corresponding to a maximum theoretical capacity of 2.43 Ah (20.25 Ah L^{-1}), during which a self-discharge rate of approximately 0.0945 Ah h^{-1} was recorded over 42 hours. While direct quantification of factors such as Fe^{2+}/Fe^{3+} crossover and hydrogen evolution were not undertaken, the observed trends provide foundational insights into the effects of operational variations on self-discharge.

Theoretically, an increase in electrolyte volume from 60 mL to 300 mL (scaling the theoretical capacity from 2.43 Ah to 12.01 Ah) is anticipated to prolong the overall reaction time. With longer reaction times, active species have more opportunity to participate fully in the redox processes, leading to higher capacity utilization. However, longer charge times also enhance the likelihood of parasitic side reactions, most notably hydrogen evolution and elevate ion crossover across the membrane. This simplified scaling estimate shows that larger electrolyte volumes experiments may increase self-discharge rates due to higher theoretical capacities. Prolonged charging times may assist in mitigating residual imbalances that drive self-discharge. This results in a more complete conversion of the active species, thereby reducing the risk of incomplete reactions that may contribute to self-discharge. This hypothesis is consistent with kinetic studies in redox flow systems and observations in vanadium redox flow batteries, where enhanced electrolyte volumes correlate with improved concentration gradients and increased crossover phenomena.[35]

Additionally, comparing cycling protocols indicates that CCCV cycling presents notable advantages over CC cycling. By regulating the voltage at an optimal cutoff (approximately 1.65–1.7 V), CCCV cycling effectively reduces overpotentials that can otherwise promote hydrogen evolution. Conversely, CC cycling sustains higher overpotentials, facilitating the acceleration of parasitic reactions that contribute to self-discharge. These observations are supported by research indicating that controlled voltage conditions can mitigate side reactions in flow batteries.[29] Furthermore, optimizing cutoff voltages for charge/discharge experiments of IRFB plays a dual role: higher charge cutoff voltages (*e.g.*, 1.9 V) maximize initial capacity but can accelerate parasitic reactions, while lower cutoff voltages (*e.g.*, 1.55 V) offer improved long-term efficiency by reducing these side reactions. In iron/iron redox flow battery, intermediate cutoff voltages (around 1.65–1.7 V) appear to strike the best balance between efficient iron plating/stripping and minimizing self-discharge-inducing reactions.

The self-discharge of iron/iron redox flow batteries represents a complex interplay among electrochemical kinetics, mass transport, and parasitic reactions like crossover and hydrogen evolution. This observation serves as a preliminary exploration into the operational influences on self-discharge. Future studies should consider employing a programmable logic controller (PLC)-based IRFB test stand to comprehensively characterize the mechanistic aspects, particularly the effects of ion crossover and hydrogen evolution. Integrating sensors for real-time monitoring of electrolyte levels, pH, conductivity, flow rate, and pressure within such a system would enable precise quantification of crossover phenomena under various pump operating modes and facilitate an in-depth analysis of pH effects on long-term self-discharge behaviour. The investigations like standby mode *etc.* are expected to provide deeper insights into the underlying mechanisms governing self-discharge, ultimately informing the development of optimized operational strategies aimed at enhancing the performance and longevity of all-iron redox flow battery systems in performance and reliability.

Conclusion & future scope

This study presents a data-driven framework for optimizing the electrochemical performance of iron/iron redox flow batteries (IRFBs) that include an integrated hydrogen recombination cell. Systematic exploration of key operational parameters including electrolyte volume, charge duration, rest interval,

© 2025 The Author(s). Published by the Royal Society of Chemistry

Open Access Article. Published on 14 July 2025. Downloaded on 4/18/2026 5:06:11 AM. This article is licensed under a Creative Commons Attribution 3.0 Unported Licence.

cutoff voltages, and charging protocols has revealed a clear operational window that maximizes energy density, maintains high efficiencies, and minimizes self-discharge. Among the conditions tested, an electrolyte volume corresponding to a theoretical capacity density of 20.25 Ah L^{-1}, a 10 min rest period between charge and discharge steps, and charge/discharge voltage cut-offs of 1.65 V and 0.30 V with current density of 25 mA cm^{-2}, respectively, emerged as optimal at room temperature. Under these conditions, IRFBs operate at intermediate charged-capacity fractions ($\approx$75–90%), a regime in which redox reaction kinetics, pH buffering capacity, and hydrogen evolution behavior reach a favorable balance. This balance leads to coulombic efficiencies exceeding 88% and energy efficiencies above 60%.

Building on these findings, several avenues for further development are proposed. First, tailoring membrane materials to enhance ion-selectivity and incorporating pH-buffering additives should be pursued to further suppress crossover of ferric species and mitigate side reactions, thereby improving long-term efficiency. Second, engineering recombination-cell flow-field geometries such as meander channels or graded porosity structures hold promises for boosting hydrogen utilization rates and accelerating recombination kinetics, which could lead to even lower self-discharge and improved operational stability. Third, incorporation of in-line electrochemical diagnostics, such as quasi-reference electrode measurements or spectroscopic sensing of Fe^{2+}/Fe^{3+} concentrations, would enable real-time tracking of electrolyte composition and battery health. Such dynamic monitoring could inform adaptive control algorithms that adjust charging currents, rest durations, or cutoff voltages on the fly to maintain optimal performance under variable load and environmental conditions.

Additional studies should also investigate the effects of temperature and flow rate on the identified optimal parameter set to ensure robust performance across a range of real-world operating scenarios. The integration of these insights into scaled multi-cell stacks and field-demonstration units will be critical to validate the laboratory findings and drive the translation of IRFB technology toward grid-scale deployment. Collectively, these efforts will refine the operational guidelines established here and accelerate the adoption of low-cost, sustainable, and durable iron/iron redox flow batteries for large-scale energy storage applications.

Conflicts of interest

The authors declare no conflicts of interest.

Data availability

Current data from the recombination cell, highlighting hydrogen evolution behavior for one representative experiment, is presented in the ESI† (Fig. S1). All other data supporting the findings of this study including raw charge/discharge voltage profiles are available from the corresponding author upon reasonable request.

References

1 S. R. Narayan, A. Nirmalchandar, A. Murali, B. Yang, L. Hoober-Burkhardt, S. Krishnamoorthy and G. K. S. Prakash, Nexgeneration aqueous flow battery chemistries, *Curr. Opin. Electrochem.*, 2019, **18**, 72–80.
2 M. Guarnieri, P. Mattavelli, G. Petrone and G. Spagnuolo, Vanadium redox flow batteries: Potentials and challenges of an emerging storage technology, *IEEE Ind. Electron. Mag.*, 2016, **10**, 20–31.
3 M. Konieczny and A. Radzicka, Synthesis of new sulfuric derivatives of allobarbital (5,5-diallylbarbituric acid) with anti-inflammatory activity, *Arch. Immunol. Ther. Exp.*, 1978, **26**, 955–957.
4 J. Janicka, P. Debiagi, A. Scholtissek, A. Dreizler, B. Epple, R. Pawellek, A. Maltsev and C. Hasse, The potential of retrofitting existing coal power plants: A case study for operation with green iron, *Appl. Energy*, 2023, **339**, 120950.
5 J. Noack, M. Berkers, J. Ortner and K. Pinkwart, The influence of some electrolyte additives on the electrochemical performance of Fe/Fe^{2+} redox reactions for iron/iron redox flow batteries, *J. Electrochem. Soc.*, 2021, **168**, 040529.
6 A. Dinesh, S. Olivera, K. Venkatesh, M. S. Santosh, M. G. Priya, Inamuddin, A. M. Asiri and H. B. Muralidhara, Iron-based flow batteries to store renewable energies, *Environ. Chem. Lett.*, 2018, **16**, 683–694.
7 Y. K. Zeng, T. S. Zhao, X. L. Zhou, L. Wei and Y. X. Ren, A novel iron-lead redox flow battery for large-scale energy storage, *J. Power Sources*, 2017, **346**, 97–102.
8 B. Yang, A. Murali, A. Nirmalchandar, B. Jayathilake, G. K. S. Prakash and S. R. Narayanan, A durable, inexpensive and scalable redox flow battery based on iron sulfate and anthraquinone disulfonic acid, *J. Electrochem. Soc.*, 2020, **167**, 060520.
9 A. K. Manohar, K. M. Kim, E. Plichta, M. Hendrickson, S. Rawlings and S. R. Narayanan, A high efficiency iron-chloride redox flow battery for large-scale energy storage, *J. Electrochem. Soc.*, 2016, **163**, A5118–A5125.
10 C. Balakrishnan, M. P. Peter, D. D. Kombarakaran, J. A. Kunjilona and J. V. Thomas, Improvement in the performance of an Fe/Fe^{2+} electrode in an all-iron redox flow battery by the addition of Zn^{2+} ions, *ChemistrySelect*, 2022, **7**, e202201222.
11 M. A. Miller, J. S. Wainright and R. F. Savinell, Iron electrodeposition in a deep eutectic solvent for flow batteries, *J. Electrochem. Soc.*, 2017, **164**, A796–A803.
12 K. Lourenssen, J. Williams, F. Ahmadpour, R. Clemmer and S. Tasnim, Vanadium redox flow batteries: A comprehensive review, *J. Energy Storage*, 2019, **25**, 100844.
13 C. Ding, H. Zhang, X. Li, T. Liu and F. Xing, Vanadium flow battery for energy storage: Prospects and challenges, *J. Phys. Chem. Lett.*, 2013, **4**, 1281–1294.
14 W. Lu, P. Xu, S. Shao, T. Li, H. Zhang and X. Li, Multifunctional carbon felt electrode with N-rich defects enables a long-cycle zinc-bromine flow battery with ultrahigh power density, *Adv. Funct. Mater.*, 2021, **31**, 2102913.

Open Access Article. Published on 14 July 2025. Downloaded on 4/18/2026 5:06:11 AM. This article is licensed under a Creative Commons Attribution 3.0 Unported Licence.

15 Z. Yuan and X. Li, Perspective of alkaline zinc-based flow batteries, *Sci. China: Chem.*, 2024, **67**, 260–275.
16 Y. Song, K. Zhang, X. Li, C. Yan, Q. Liu and A. Tang, Tuning the ferrous coordination structure enables a highly reversible Fe anode for long-life all-iron flow batteries, *J. Mater. Chem. A*, 2021, **9**, 26354–26361.
17 A. S. N. Murthy and T. Srivastava, Fe(III)/Fe(II)–ligand systems for use as negative half-cells in redox-flow cells, *J. Power Sources*, 1989, **27**, 119–126.
18 L. W. Hruska and R. F. Savinell, Investigation of factors affecting performance of the iron-redox battery, *J. Electrochem. Soc.*, 1981, **128**, 18–25.
19 J. Noack, M. Wernado, N. Roznyatovskaya, J. Ortner and K. Pinkwart, Studies on Fe/Fe redox flow batteries with recombination cell, *J. Electrochem. Soc.*, 2020, **167**, 160527.
20 N. Yensen and P. B. Allen, Open-source all-iron battery for renewable energy storage, *HardwareX*, 2019, **6**, e00072.
21 K. L. Hawthorne, J. S. Wainright and R. F. Savinell, Studies of iron-ligand complexes for an all-iron flow battery application, *J. Electrochem. Soc.*, 2014, **161**, A1662–A1671.
22 M. Furquan, S. Ali, S. R. Hussaini, Z. M. Bhat, M. A. Z. G. Sial, A. S. Alzahrani, Z. H. Yamani and M. Qamar, Electrolyte additives and 3D X-ray tomography study of all-iron redox flow batteries in a full-cell configuration for high-capacity retention, *Energy Fuels*, 2024, **38**, 4699–4710.
23 H. Prifti, A. Parasuraman, S. Winardi, T. M. Lim and M. Skyllas-Kazacos, Membranes for redox flow battery applications, *Membranes*, 2012, **2**, 275–306.
24 N. Sinclair, M. Vasil, C. Kellamis, E. A. Nagelli, J. Wainright, R. Savinell and G. E. Wnek, Membrane considerations for the all-iron hybrid flow battery, *J. Electrochem. Soc.*, 2023, **170**, 050516.
25 V. Tam and J. Wainright, Electrochemical behavior of low loading slurry electrodes for redox flow batteries, *J. Electrochem. Soc.*, 2023, **170**, 010538.
26 S. Selverston, R. F. Savinell and J. S. Wainright, In-tank hydrogen–ferric ion recombination, *J. Power Sources*, 2016, **324**, 674–678.
27 Z. Siroma, S. Yamazaki, M. Yao, N. Fujiwara, M. Asahi and T. Ioroi, Redox flow battery in combination with hydrogen evolution/oxidation electrode, *ECS Meet. Abstr.*, 2012, 404MA2012-02.
28 Y. K. Zeng, T. S. Zhao, X. L. Zhou, J. Zou and Y. X. Ren, A hydrogen–ferric ion rebalance cell operating at low hydrogen concentrations for capacity restoration of iron-chromium redox flow batteries, *J. Power Sources*, 2017, **352**, 77–82.
29 B. S. Jayathilake, E. J. Plichta, M. A. Hendrickson and S. R. Narayanan, Improvements to the coulombic efficiency of the iron electrode for an all-iron redox-flow battery, *J. Electrochem. Soc.*, 2018, **165**, A1630–A1638.
30 Z. Yuan and X. Li, Perspective of alkaline zinc-based flow batteries, *Sci. China: Chem.*, 2024, **67**, 260–275.
31 Y. Shi, C. Eze, B. Xiong, W. He, H. Zhang, T. M. Lim, A. Ukil and J. Zhao, Recent development of membrane for vanadium redox flow battery applications: A review, *Appl. Energy*, 2019, **238**, 202–224.
32 A. Khor, P. Leung, M. R. Mohamed, C. Flox, Q. Xu, L. An, R. G. A. Wills, J. R. Morante and A. A. Shah, Review of zinc-based hybrid flow batteries: From fundamentals to applications, *Mater. Today Energy*, 2018, **8**, 80–108.
33 Y. Qiao, Y. He, K. Jiang, Y. Liu, X. Li, M. Jia, S. Guo and H. Zhou, High-voltage Li-ion full-cells with ultralong term cycle life at elevated temperature, *Adv. Energy Mater.*, 2018, **8**, 1802322.
34 B. Li, L. Li, W. Wang, Z. Nie, B. Chen, X. Wei, Q. Luo, Z. Yang and V. Sprenkle, Fe/V redox flow battery electrolyte investigation and optimization, *J. Power Sources*, 2013, **229**, 1–5.
35 N. Remmler and M. Bron, Recent progress in our understanding of the degradation of carbon-based electrodes in vanadium redox flow batteries – Current status and next steps, *ChemElectroChem*, 2024, **11**, e202400127.
36 R. Patel, Q. Huang, B. Li, A. Crawford, B. M. Sivakumar, C. Song, Z. Jiang, A. Platt, K. Fatih and D. Reed, Reliability studies of vanadium redox flow batteries: Upper limit voltage effect, *RSC Adv.*, 2024, **14**, 34381–34389.
37 D. P. Trudgeon, A. Loh, H. Ullah, X. Li, V. Yufit, N. Brandon, M. Liu and L. Kong, The influence of zinc electrode substrate, electrolyte flow rate and current density on zinc–nickel flow cell performance, *Electrochim. Acta*, 2021, **373**, 137890.

© 2025 The Author(s). Published by the Royal Society of Chemistry